Analysis and Design of *LCL* Resonant Tank With Reduced Reactive Power for Bidirectional On-Board Charger Applications Utilizing Time-Domain Model

Lie Zhao, *Member, IEEE*, Yunqing Pei, *Member, IEEE*, Laili Wang, *Senior Member, IEEE*, Long Pei, *Member, IEEE*, Zhixiang Li, *Member, IEEE*, and Wei Cao, *Member, IEEE*

***Abstract*—To address the wide voltage conversion requirements in the field of battery charging, the *LCL* resonant tank adopting pulse frequency modulation is investigated utilizing the time-domain model (TDM) in this article. *LCL* exhibits similar soft switching characteristics and enhanced voltage gain regulation capability with a simpler resonant tank than the existing classic *CLLC*. The operating principles, mode distribution, and power transfer properties of *LCL* during bidirectional operations are presented and analyzed in detail utilizing TDM. By incorporating TDM, the low accuracy deficiency of the first harmonic approximation for wide voltage applications is completely eliminated, and the implementation of full-range zero-voltage switching (ZVS) with time-domain accuracy becomes feasible. An *LCL* resonant parameters optimization method that is capable of providing the required voltage gain and guaranteeing the achievement of ZVS with reduced reactive power under desired load conditions during bidirectional operations is proposed. Finally, the revealed experimental results from a 1-kW prototype validated the correctness of the TDM theoretical analysis and the effectiveness of the proposed optimization method. The optimized prototype achieves the designed 1.8× voltage gain within a narrow switching frequency range of 88.7–120 kHz and a peak efficiency of 97.306%.**

***Index Terms*—*LCL* resonant tank, time-domain model (TDM), wide voltage conversion, zero-current switching (ZCS), zero-voltage switching (ZVS).**

I. Introduction

With the popularity and penetration of electric vehicles (EVs) in the automotive industry, the demand for charging infrastructure has been growing significantly [1], [2]. High power density, wide soft-switching range, and wide voltage conversion range are the core requirements of battery chargers in EV charging applications [3], [4], [5]. In addition, the next-generation on-board chargers (OBCs) are expected to deliver bidirectional power flow to perform vehicle-to-grid functions for advanced grid support features, such as peak cutting and valley filling [2]. In general, the bidirectional OBC architecture consists of an ac–dc power factor correction (PFC) stage followed by an isolated dc–dc stage that regulates the battery voltage and provides high-frequency galvanic isolation [6]. Considering that the research on the front-end PFC stage is relatively mature, only the isolated dc–dc stage of OBC is discussed in this article.

Among various topologies investigated in the literature for the dc–dc stage of OBCs, resonant converters are a favorable candidate. A bidirectional series resonant converter (SRC) with a basic series *LC* resonant network is the simplest resonant tank in the structure. However, SRC fails to provide voltage gain larger than unity, severely limiting its application in the field of bidirectional OBC. An *LLC* resonant tank with inherent capabilities of achieving soft switching to minimize switching losses allows high-frequency operation while maintaining high conversion efficiencies [7], [8], [9]. Nevertheless, the *LLC* resonant tank is inherently asymmetric and behaves as a conventional SRC during reverse power flow with voltage gain less than unity [10]. However, this can be tackled with the bidirectional *CLLC* resonant tank derived from *LLC* with a symmetric structure [11]. However, to address the wide voltage range of battery charger applications, *CLLC* requires an extensive frequency modulation range that deviates from the resonant frequency, significantly compromising its efficiency, especially under light-load conditions [10], [12]. To overcome this demerit, a CLTC resonant tank is presented with decent gain characteristics and high efficiency over all load ranges with a relatively narrow frequency modulation range [13]. However, the introduction of an auxiliary transformer leads to more core loss and more complex design considerations. To obtain similar performance with a relatively simple resonant tank, an *LCCL* resonant tank is proposed with respect to *CLLC* through the duality theory [14], which maintains fairly flat efficiency and narrow frequency modulation range under all load conditions. Nevertheless, the design considerations of *LCCL* are quite complicated, which hinders its engineering application to some extent.

The dual-active-bridge (DAB) converter has also been investigated as the dc–dc stage of OBCs [15], which requires

Manuscript received 19 July 2023; revised 10 November 2023; accepted 16 December 2023. Date of publication 22 December 2023; date of current version 16 February 2024. This work was supported by the Shaanxi Science and Technology Innovation Team Program under Grant 2022TD-64. Recommended for publication by Associate Editor O. Lucia. *(Corresponding authors: Yunqing Pei; Laili Wang.)*

The authors are with the State Key Laboratory of Electrical Insulation and Power Equipment, Xi'an Jiaotong University, Xi'an 710049, China (e-mail: winter_zl@stu.xjtu.edu.cn; peiyq@mail.xjtu.edu.cn; llwang@mail.xjtu.edu.cn; pl0823@stu.xjtu.edu.cn; lizhixiang951206@stu.xjtu.edu.cn; caowei@stu.xjtu.edu.cn).

Color versions of one or more figures in this article are available at https://doi.org/10.1109/TPEL.2023.3346174.

Digital Object Identifier 10.1109/TPEL.2023.3346174

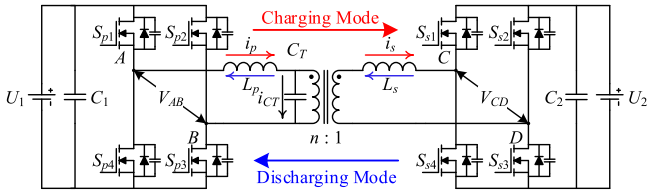

Fig. 1. Schematic of the bidirectional *LCL* resonant tank.

fewer passive components in contrast to conventional resonant topologies, consisting of two full-bridges isolated by a high-frequency transformer with a series inductor. Moreover, DAB implements bidirectional power flow and zero-voltage switching (ZVS) exclusively through single-phase-shift (SPS) control at fixed switching frequency, which is desirable for high efficiency and high power density applications [16]. Nonetheless, excessive circulating energy and possible loss of ZVS under light-load conditions severely limit a DAB converter to maintain high efficiency over a wide voltage range [17]. Therefore, various modulation schemes have been developed from single to triple degrees of freedom to enlarge the related soft-switching range and lower the circulating energy [18], [19], [20]. Besides the most fundamental SPS, dual-phase-shift (DPS), extended-phase-shift (EPS), and triple-phase-shift (TPS) controls were introduced to minimize switching loss and to reduce the reactive power under light-load conditions [21], [22]. Moreover, pulse frequency modulation (PFM) is also combined with multi-degree-of-freedom phase-shift (PS) control to manipulate the power conversion of DAB [23], [24]. While these complex control strategies offer more degrees of control freedom and thus a wider range of optimization possibilities, they also result in more complex implementations and higher hardware costs. In addition, the related power conversion performance of DAB remains inferior to that of bidirectional resonant topologies in the application scenario with a wide range of output voltage or load conditions of OBC [12], [25].

Besides the series-inductor-based DAB discussed above, more and more efforts are focused on resonant DAB utilizing second or higher order resonant tanks. The superiority of higher order resonant networks over single inductor structures is the extended soft-switching range and reduced root-mean-square current, resulting in reduced conduction losses and improved transformer utilization. This is also the essential distinction between the aforementioned resonant converter (e.g., *LLC*, *CLLC,* and *LCCL*) and the conventional DAB topology. Among the various reported resonant DABs, the *LCL* resonant network depicted in Fig. 1 is a promising type due to its symmetrical and concise structure, which is suitable for bidirectional operations. Traditionally, the series-inductor-based DAB is analyzed with the piecewise linear methods. However, within the resonant DAB, current waveforms become more sinusoidal. Accordingly, similar to resonant topologies, resonant DAB is generally investigated utilizing first harmonic approximation (FHA) [26], [27], [28], [29], [30], which considers only the fundamental components of the resonant tank's response while neglecting corresponding high-order components [31]. The salient disadvantage of the FHA is that its accuracy deteriorates when the current waveform is not so sinusoidal or the switching frequency deviates from the resonant frequency. Unfortunately, these scenarios are frequently encountered in battery charging applications since the battery voltage varies considerably throughout the charging and discharging process. Therefore, the time-domain model (TDM) is utilized in this article to analyze the characteristics of the *LCL* resonant tank for bidirectional OBC application. The most significant advantage of TDM over FHA is that the time-domain response of the resonant tank is accurately obtained irrespective of whether the current waveforms are sufficiently sinusoidal or not. As a result, more precise power transfer characteristics can be derived and the achievement of full-range ZVS in terms of time-domain accuracy is guaranteed. In addition, this article adopts PFM to excite the *LCL* resonant tank. Therefore, the rectifier-side switches are naturally zero-current switching (ZCS) as the conventional resonant topologies and only the ZVS implementation of inverting-side switches demands additional design.

To cope with the wide voltage range of bidirectional OBC applications, the *LCL* resonant tank adopting PFM is investigated utilizing TDM in this article. With the proposed method for optimizing parameters, the designed prototype achieves the required 1.8× voltage gain range within a narrow switching frequency range of 88.7–120 kHz and implements the full range of ZVS under the entire load conditions (0–100%), well demonstrating its excellent performances. The rest of this article is organized as follows. The basic operating principles of the *LCL* resonant tank are reviewed in Section II. In Section III, TDM is utilized to investigate an *LCL* converter during bidirectional operations. Subsequently, an *LCL* resonant parameters optimization method that is capable of providing the required wide voltage range of the battery charger field and guaranteeing the achievement of ZVS with reduced reactive power under desired load conditions during bidirectional operations is developed in Section IV. Experimental results from a 1-kW prototype are revealed in Section V to confirm the correctness of the TDM theoretical analysis and the effectiveness of the proposed parameters optimization method. Finally, the conclusions are drawn in Section VI.

II. Operating Principles of *LCL* Resonant Tank

For the *LCL* resonant tank depicted in Fig. 1, the following definitions are introduced:

$$\begin{cases} h = n^2 L_s / L_p \\ f_r = \dfrac{1}{2\pi\sqrt{\frac{L_p n^2 L_s}{L_p + n^2 L_s} C_T}} = \sqrt{\dfrac{h+1}{h}} \dfrac{1}{2\pi\sqrt{L_p C_T}} \\ \quad = \sqrt{h+1} \dfrac{1}{2\pi\sqrt{n^2 L_s C_T}} \end{cases} \tag{1}$$

where h represents the symmetry coefficient and f_r denotes the resonant frequency of the *LCL* resonant tank.

PFM is adopted to excite the *LCL* resonant tank and regulate the output voltage with switching frequency around resonant frequency f_r. Specifically, in charging mode, the primary-side switches S_{p1} and S_{p3} and S_{p2} and S_{p4} are driven at complementary 50% duty cycle, while the body diodes of secondary-side

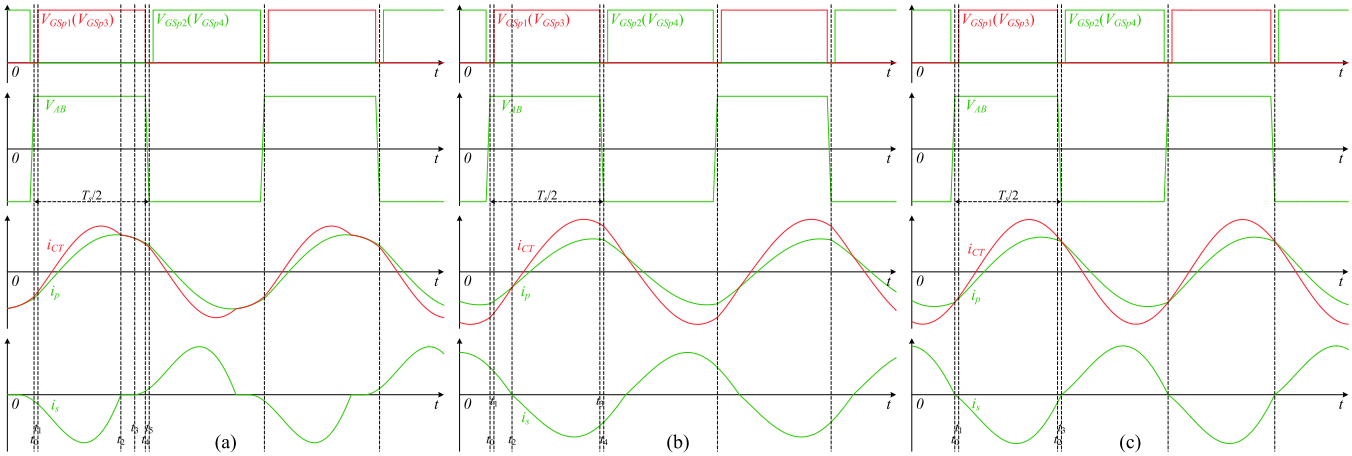

Fig. 2. Typical waveforms of *LCL*. (a) Below resonant frequency (NOP mode). (b) Above resonant frequency (NP mode). (c) Resonant frequency (N mode).

switches S_{s1} and S_{s3} and S_{s2} and S_{s4} are employed for rectification. The principle remains similar in discharging mode, except that secondary-side switches S_{s1} and S_{s3} and S_{s2} and S_{s4} are driven at complementary 50% duty cycle and the primary-side switches S_{p1} and S_{p3} and S_{p2} and S_{p4} operate as rectifiers.

Typical waveforms of *LCL* operating below and above resonant frequency f_r are provided in Fig. 2(a) and (b), respectively. Furthermore, Fig. 2(c) depicts the typical waveform of *LCL* operating exactly at the resonant frequency, where V_{GSpq} (q = 1, 2, 3, 4) is the drive signal of S_{pq} (q = 1, 2, 3, 4), V_{AB} denotes the inverting voltage of the primary resonant tank, i_p and i_s represent the resonant current of primary and secondary sides, respectively, i_{CT} indicates the resonant current of C_T, and T_s indicates the switching period.

Due to the similarity of multiple stages in Fig. 2(a)–(c), only Fig. 2(a) is described in detail to interpret the operation principles of *LCL*. The corresponding equivalent circuits for each stage are illustrated in Fig. 3.

Stage 1 [t_0, t_1)*:* During the dead band, after the junction capacitors of inverting-side switches have been adequately charged or discharged, the resonant current i_p starts to flow through the body diodes of S_{p1} and S_{p3} at time t_0.

Stage 2 [t_1, t_2)*:* At time t_1, S_{p1} and S_{p3} turned ON under ZVS conditions, allowing energy to be delivered to the rectifier side via the resonant tank. Meanwhile, resonant current i_s flows through S_{s2} and S_{s4} is proportional to the difference between i_p and i_{CT}.

Stage 3 [t_2, t_3)*:* After reaching its peak, i_{CT} starts to decrease and becomes equal to the increasing resonant current i_p at time t_2. Meanwhile, the resonant current i_s gradually resonates to 0, causing S_{s2} and S_{s4} to turn OFF under ZCS conditions. The separation of L_s from the resonant tank results in the free resonance of L_p and C_T after time t_2.

Stage 4 [t_3, t_4)*:* At time t_3, the voltage of C_T resonates to exceeds nU_2 and S_{s1} and S_{s3} start to conduct, causing the resonant element on the rectifier side to resonate with the inverting-side resonant tank again.

Stage 5 [t_4, t_5)*:* With S_{p1} and S_{p3} turned OFF at time t_4, i_p begins to discharge the junction capacitors of S_{p2} and S_{p4} and

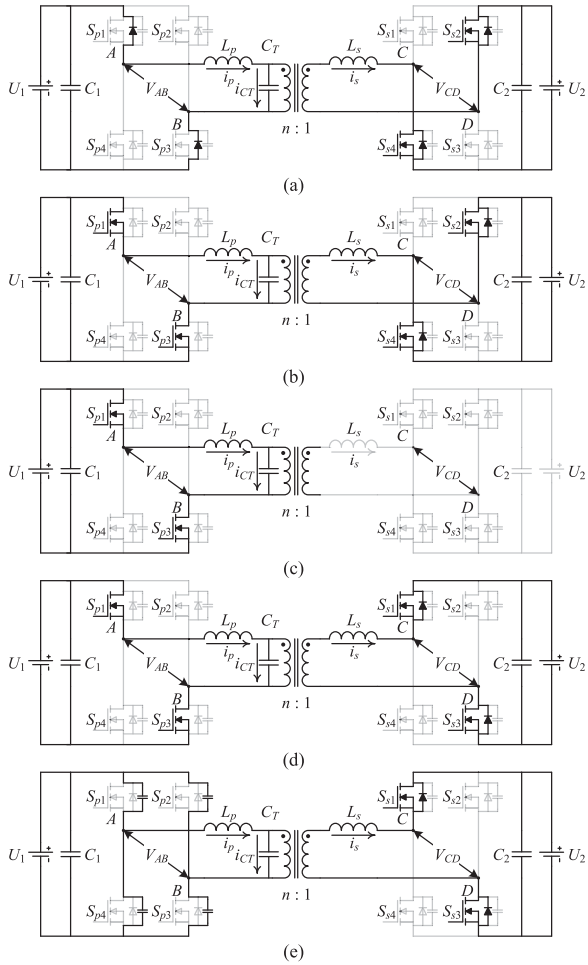

Fig. 3. Equivalent circuits for each stage of *LCL* operating below resonance-like frequency. (a) Stage 1. (b) Stage 2. (c) Stage 3. (d) Stage 4. (e) Stage 5.

charge that of S_{p1} and S_{p3} simultaneously. At the end of *Stage* 5, the drain–source voltage of S_{p2} and S_{p4} drops to 0 and that of S_{p1} and S_{p3} reaches U_1. Until time t_5, the polarity of the inverting voltage V_{AB} has flipped from U_1 to $-U_1$, marking

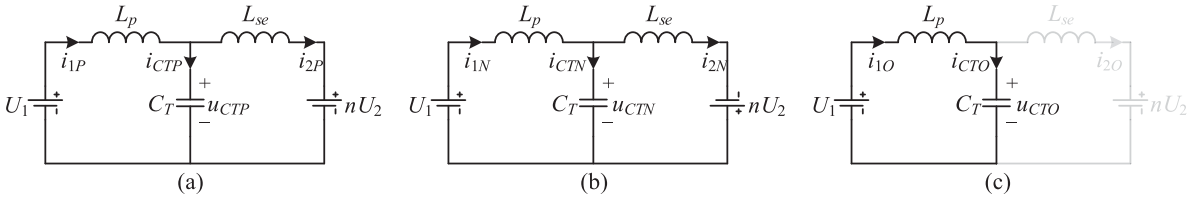

Fig. 4. Equivalent circuit of *LCL* resonant tank in positive half-cycle. (a) P stage. (b) N stage. (c) O stage.

the end of the positive half-cycle, and initiating the subsequent negative half-cycle.

Clearly, the response of the *LCL* resonant tank under PFM excitation is quite similar to the typical response of *CLLC*. In addition, *LCL* also behaves as a constant voltage source under resonant frequency f_r excitation (as will be explained later). Therefore, *LCL* offers soft-switching capability similar to that of *CLLC* (e.g., ZVS for inverting-side switches and ZCS for rectifier-side switches).

III. Characterizing *LCL* Resonant Tank Utilizing TDM

A. Forward Operation

As illustrated in Fig. 2, the responses of *LCL* are symmetrical in both half-cycles under PFM excitation with a complementary 50% duty cycle. For convenience, the following analysis takes the positive half-cycle when V_{AB} is positive as a demonstration.

1) Resonant Stage Analysis: The complexity of *LCL* operation stems from its multiple resonance mechanisms. In addition to the resonance formed by L_p, C_T, and L_s, L_p and C_T also resonate when the secondary-side switches are all OFF. Depending on the differences in parameter specifications, switching frequency, and load conditions, *LCL* could sequentially go through multiple resonant stages during the positive half-cycle. The various resonant stages are classified according to the conduction states of rectifier-side body diodes as P stage (the body diodes of S_{s1} and S_{s3} turn ON), N stage (the body diodes of S_{s2} and S_{s4} turn ON), and O stage (no body diodes turn ON) [8], [31]. The associated equivalent circuits are depicted in Fig. 4, where $L_{se} = n^2 L_s$.

In stage P, V_{CD} of the resonant tank is clamped to U_2, and the equivalent circuit can be described as a system of three-order differential equations as

$$\begin{cases} U_1 = L_p \frac{di_{1P}}{dt} + u_{CTP} \\ u_{CTP} = L_{se} \frac{di_{2P}}{dt} + nU_2 \\ i_{1P} = C_T \frac{du_{CTP}}{dt} + i_{2P} \end{cases}. \tag{2}$$

The corresponding normalizations are outlined in Table I to facilitate the relevant derivations. In particular, there are four pivotal normalization bases as

$$\omega_{\text{base}} = (L_p C_T)^{-1/2} = 2\pi f_{\text{base}}, \quad U_{\text{base}} = U_1$$
$$Z_{\text{base}} = \sqrt{L_p / C_T}, \quad I_{\text{base}} = U_{\text{base}} / Z_{\text{base}}. \tag{3}$$

By solving (2), the normalized waveforms of the P stage are derived in (4) shown at the bottom of next page, where $h_1 = ((h+1)/h)^{1/2} = \omega_r/\omega_{\text{base}}$ is the normalized resonant frequency. The subscript P denotes the P stage, and j_{1P0}, m_{CTP0}, and j_{2P0} represent the initial values of $j_{1P}(\theta)$, $m_{CTP}(\theta)$, and $j_{2P}(\theta)$, respectively.

TABLE I
Abbreviations and Normalizations

Circuit Variables	Symbol	Normalized Variables
Characteristic frequency	$\omega_{\text{base}}=(L_pC_T)^{-1/2}$	-
Resonant frequency	$\omega_r=2\pi f_r$	$\omega_r=((h+1)/h)^{1/2}\omega_{\text{base}}$
Characteristic impedance	$Z_{\text{base}}=(L_p/C_T)^{1/2}$	-
Voltage gain	$M=nU_2/U_1$	-
Time	t	$\theta=\omega_{\text{base}}t$
Switching frequency	$f_s=1/T_s$	$f_n=f_s/f_{\text{base}}$
Half-cycle	$T_s/2=1/(2f_s)$	$\gamma=\pi/f_n$
Primary resonant current	$i_1(t)$	$j_1(\theta)=Z_{\text{base}}i_1(t)/U_1$
Secondary resonant current	$i_2(t)$	$j_2(\theta)=Z_{\text{base}}i_2(t)/U_1$
Parallel capacitor voltage	$u_{CT}(t)$	$m_{CT}(\theta)=u_{CT}(t)/U_1$
Parallel capacitor current	$i_{CT}(t)$	$j_{CT}(\theta)=Z_{\text{base}}i_{CT}(t)/U_1$
Reflected output voltage	nU_2	M

Similar to the P stage, the normalized waveforms of the N stage are obtained in (5) shown at the bottom of the next page. Accordingly, the subscript N indicates the N stage, and j_{1N0}, m_{CTN0}, and j_{2N0} refer to the initial values of $j_{1N}(\theta)$, $m_{CTN}(\theta)$, and $j_{2N}(\theta)$, respectively.

For stage O, the equivalent circuit degenerates into a basic *LC* series network. The corresponding normalized waveforms are provided in (6), where subscript O represents the O stage, and j_{1O0} and m_{CTO0} are the initial values of $j_{1O}(\theta)$ and $m_{CTO}(\theta)$, respectively.

$$\begin{cases} j_{1O}(\theta) = (1 - m_{CTO0})\sin(\theta) + j_{1O0}\cos(\theta) \\ m_{CTO}(\theta) = 1 + j_{1O0}\sin(\theta) + (m_{CTO0} - 1)\cos(\theta) \\ j_{2O}(\theta) = 0 \end{cases}. \tag{6}$$

2) Analysis of Operation Modes: Depending on the different sequential combinations of the three resonant stages (P, N, and O), nine meaningful operation modes exist for *LCL* resonant tank: NO, NOP [i.e., Fig. 2(a)], NP, PN [i.e., Fig. 2(b)], PON, ON, ONO, N [i.e., Fig. 2(c)], and O. The relevant characteristics of each mode are summarized in Table II. To facilitate subsequent description, the switching frequency range is grouped into three separate regions: above the resonant region ($f_n > h_1$) (ARR), resonant frequency ($f_n = h_1$), and below the resonant region ($1 < f_n < h_1$) (BRR).

As illustrated in Fig. 4, the inverting side and the rectifier side are disconnected during the O stage, and energy can only be delivered to load in P and N stages. Therefore, the normalized output current $I_{\text{out\_}n}$ of *LCL* is obtained in (7), where $\theta_{P0}(\theta_{N0})$

TABLE II
OPERATION CHARACTERISTICS OF *LCL* RESONANT TANK

	BRR: $1<f_n<h_1$					$f_n=h_1$			ARR: $f_n>h_1$				
Mode	NP	NOP	NO	ONO	O	N	ONO	O	PN	PON	ON	ONO	O
Inverting switches	ZVS/ZCS	ZVS/ZCS	ZVS/ZCS	ZVS	ZVS	ZVS	ZVS	ZVS	ZVS	ZVS	ZVS	ZVS	ZVS
Rectifier switches	HS	ZCS	ZCS	ZCS	OFF	ZCS	ZCS	OFF	HS	ZCS	ZCS	ZCS	OFF
Voltage gain	Indefinite		$M>h$			$M\equiv h$	$M>h$		$M<h$			Indefinite	
I_{out_n}	Large→small				0	$[I_{b\_n}, +\infty)$	$(0, I_{b\_n})$	0	Large→small				0

Hard switching: HS; zero-voltage switching: ZVS; zero-current switching: ZCS.

and $\theta_P(\theta_N)$ represent the beginning and end of the P(N) stage, respectively. Furthermore, the normalized output power $P_{\text{out\_}n}$ is derived in (8).

$$\begin{aligned} I_{\text{out\_}n} &= f_n \int_0^{\pi/f_n} |j_2(\theta)| d\theta/\pi \\ &= f_n \left(\int_{\theta_{P0}}^{\theta_P} j_{2P}(\theta) d\theta - \int_{\theta_{N0}}^{\theta_N} j_{2N}(\theta) d\theta \right) \Big/ \pi \end{aligned} \tag{7}$$

$$\begin{aligned} P_{\text{out\_}n} = M I_{\text{out\_}n} = M f_n \Bigg(& \int_{\theta_{P0}}^{\theta_P} j_{2P}(\theta) d\theta \\ & - \int_{\theta_{N0}}^{\theta_N} j_{2N}(\theta) d\theta \Bigg) \Big/ \pi. \end{aligned} \tag{8}$$

Each operation mode is subject to several constraints. First, considering that the energy cannot be changed suddenly, the inductor current and capacitor voltage (e.g., j_1, j_2, and m_{CT}) should satisfy the principle of continuity. Second, the steady-state response of the resonant tank should conform to the previously discussed half-wave symmetry principle. In addition, the resonant current of the rectifier side is not only continuous but also differentiable when the resonant tank is commuting from the O stage to P or N stage (this condition only applies to NO, NOP, PON, ON, and ONO). NP mode is picked as an example to demonstrate these aforementioned constraints in the following:

$$\begin{cases} j_{1N}(\theta_N) = j_{1P}(\theta_{P0}), j_{2N}(\theta_N) = 0 \\ m_{CTN}(\theta_N) = m_{CTP}(\theta_{P0}) \\ j_{1N}(\theta_{N0}) + j_{1P}(\theta_P) = 0, j_{2N}(\theta_{N0}) + j_{2P}(\theta_P) = 0 \\ m_{CTN}(\theta_{N0}) + m_{CTP}(\theta_P) = 0 \\ \theta_{N0} = 0, \theta_{P0} = \theta_N, \theta_P = \pi/f_n \\ \int_{\theta_{N0}}^{\theta_P} |j_2(\theta)| d\theta = \int_{\theta_{P0}}^{\theta_P} j_{2P}(\theta) d\theta - \int_{\theta_{N0}}^{\theta_N} j_{2N}(\theta) d\theta = \pi I_{\text{out\_}n}/f_n \end{cases} \tag{9}$$

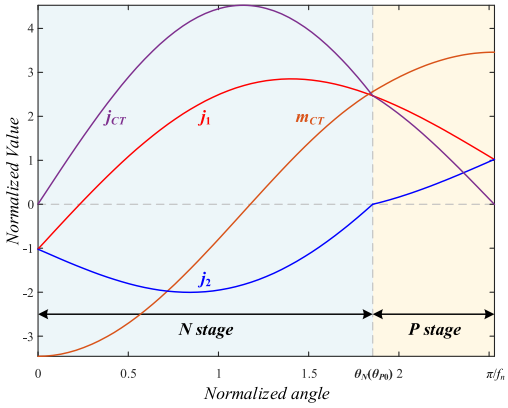

Fig. 5. Time-domain waveforms of NP mode.

where θ_N or θ_{P0} indicates the moment of commutation from the N stage to P stage. During the positive half-cycle of NP mode, start by N stage that maintains for $[0, \theta_N]$, followed by P stage operating for the rest of the half-cycle $[\theta_{P0}, \pi/f_n]$. Accordingly, nonlinear transcendental equations similar to (9) can be derived for other modes as well. However, the closed-form analytical solution exists only for N mode, and for other modes, only numerical solutions can be acquired. In summary, the precise time-domain response of the *LCL* resonant tank for each mode can be obtained accurately utilizing TDM. As a demonstration, the time-domain waveform of NP mode obtained via TDM is illustrated in Fig. 5.

The closed-form analytical solutions of N mode are provided in (10) and (11). Besides, as depicted in Fig. 2(c), $j_{2N}(\theta)$ of N mode should be nonpositive during the positive half-cycle. Therefore, the load condition of N mode (e.g., $I_{\text{out\_}n}$) should not be less than a critical value. Otherwise, the resonant tank

$$\begin{cases} j_{1P}(\theta) = \frac{h j_{2P0} + j_{1P0}}{h+1} - \frac{M-1}{h+1}\theta + \frac{h+M-(h+1)m_{CTP0}}{h_1(h+1)} \sin(h_1\theta) + \frac{h(j_{1P0}-j_{2P0})}{h+1} \cos(h_1\theta) \\ m_{CTP}(\theta) = \frac{h+M}{h+1} + \frac{j_{1P0}-j_{2P0}}{h_1} \sin(h_1\theta) + \left(m_{CTP0} - \frac{h+M}{h+1} \right) \cos(h_1\theta) \\ j_{2P}(\theta) = \frac{h j_{2P0} + j_{1P0}}{h+1} - \frac{M-1}{h+1}\theta + \frac{h_1((h+1)m_{CTP0}-h-M)}{(h+1)^2} \sin(h_1\theta) - \frac{j_{1P0}-j_{2P0}}{h+1} \cos(h_1\theta) \end{cases} \tag{4}$$

$$\begin{cases} j_{1N}(\theta) = \frac{h j_{2N0} + j_{1N0}}{h+1} - \frac{-M-1}{h+1}\theta + \frac{h-M-(h+1)m_{CTN0}}{h_1(h+1)} \sin(h_1\theta) + \frac{h(j_{1N0}-j_{2N0})}{h+1} \cos(h_1\theta) \\ m_{CTN}(\theta) = \frac{h-M}{h+1} + \frac{j_{1N0}-j_{2N0}}{h_1} \sin(h_1\theta) + \left(m_{CTN0} - \frac{h-M}{h+1} \right) \cos(h_1\theta) \\ j_{2N}(\theta) = \frac{h j_{2N0} + j_{1N0}}{h+1} - \frac{-M-1}{h+1}\theta + \frac{h_1((h+1)m_{CTN0}-h+M)}{(h+1)^2} \sin(h_1\theta) - \frac{j_{1N0}-j_{2N0}}{h+1} \cos(h_1\theta) \end{cases} \tag{5}$$

TABLE III
BOUNDARY CONDITIONS OF OPERATION MODES

Mode boundaries	Solving mode	Constraint
ONO/NOP	NO	$m_{CTN}(\theta_{N0})$=-M or $m_{CTO}(\pi/f_n)$=M
NOP/NP	NP	$m_{CTN}(\theta_{P0})$=M
ONO/PON	ON	$m_{CTO}(\theta_{N0})$=-M
PON/PN	PN	$m_{CTP}(\theta_{N0})$=-M

will enter the ONO mode. This critical load condition of $I_{\text{out\_}n}$ is indicated as I_{b_n} and is provided in (12).

$$\begin{cases} j_{1N0} = -\pi\sqrt{h\,(1+h)}\Big/2 \\ m_{CTN0} = -\pi I_{\text{out\_}n}\sqrt{h\,(1+h)}\Big/2 \\ j_{2N0} = 0 \\ M = h \end{cases} \tag{10}$$

$$\begin{cases} j_{1N}(\theta) = -\frac{\pi}{2h_1} + \theta + \frac{\pi h I_{out\_n}}{2}\sin(h_1\theta) - \frac{\pi h}{2h_1}\cos(h_1\theta) \\ m_{CTN}(\theta) = -\frac{1}{2}\pi\left(h\sin(h_1\theta) + I_{out\_n}\sqrt{h\,(h+1)}\cos(h_1\theta)\right) \\ j_{2N}(\theta) = -\frac{\pi}{2h_1} + \theta - \frac{\pi I_{out\_n}}{2}\sin(h_1\theta) + \frac{\pi}{2h_1}\cos(h_1\theta) \end{cases} \tag{11}$$

$$I_{b\_n} = \frac{2}{\pi h_1}. \tag{12}$$

3) Mode Boundaries and Distribution: As Table II states, different modes have different frequency ranges, voltage gain, and load conditions (e.g., output current). Therefore, identifying the mode boundaries and distribution is crucial to apply the correct mode equations according to the frequency and load conditions. The mode boundaries could be a critical case of operation modes or a unique boundary mode, e.g., the mode boundary between NOP and NP is the critical NP mode that V_{CD} reaches U_2 exactly at the end of the N stage. Hence, this boundary can be obtained by solving the critical NP mode equations. In addition to the regular mode boundaries, there are three boundary modes: NO boundary mode between ONO and NOP, ON boundary mode between ONO and PON, and critical O mode under zero-load conditions. All the boundary conditions are listed in Table III. Fig. 6 portrays the typical mode boundaries and distribution of the *LCL* resonant tank on the f_n–M plane, which depends only on parameter h.

For critical O mode under zero-load condition, no energy is transferred to the rectifier side and only reactive power circulates in the inverting-side resonant tank. The analytical solution of critical O mode under zero load is given as follows:

$$\begin{cases} j_{1O0} = -\tan\left(\frac{\pi}{2f_n}\right) \\ m_{CTO0} = 0 \end{cases} \tag{13}$$

$$\begin{cases} j_{1O}(\theta) = \sin(\theta) - \tan\left(\frac{\pi}{2f_n}\right)\cos(\theta) \\ m_{CTO}(\theta) = 1 - \tan\left(\frac{\pi}{2f_n}\right)\sin(\theta) - \cos(\theta) \end{cases}. \tag{14}$$

Note that *LCL* is usually designed to operate in the ZVS region for power efficiency concerns. Therefore, the normalized switching frequency f_n is set to be greater than 1 to guarantee $j_{1O0} < 0$.

The reason why the rectifier-side body diodes are all OFF in O mode is that the peak voltage of the parallel capacitor C_T never exceeds the output voltage. Therefore, the gain curve M_O of critical O mode is derived as

$$M_O = |m_{CTO}(\theta)|_{\max} = \left|m_{CTO}\left(\frac{\pi}{2f_n}\right)\right| = \sec\left(\frac{\pi}{2f_n}\right) - 1. \tag{15}$$

4) Comparison of Gain Characteristics With Other Bidirectional Resonant Topologies: Since only the gain curve of the critical O mode can be expressed with a closed-form analytical solution, the gain characteristics of the critical O mode were selected as a criterion to evaluate the gain capability of different bidirectional resonant topologies (e.g., *CLLC* [12] and *LCCL* [14]). Referring to [12], the gain characteristic of the critical O mode for *CLLC* is provided in (16), where k_L denotes the ratio of resonant inductance to magnetizing inductance on the inverting side. Similarly, the gain characteristic of the critical O mode for *LCCL* is derived in [14] and rewritten in (17), where k_C represents the ratio of the parallel resonant capacitance to resonant capacitance on the inverting side.

$$M_{O\_CLLC} = \frac{1}{k_L+1}\sec\left(\sqrt{\frac{k_L}{k_L+1}}\pi\Big/(2f_n)\right) \tag{16}$$

$$M_{O\_LCCL} = \frac{1}{k_C+1}\left(\sec\left(\sqrt{\frac{k_C+1}{k_C}}\pi\Big/(2f_n)\right) - 1\right). \tag{17}$$

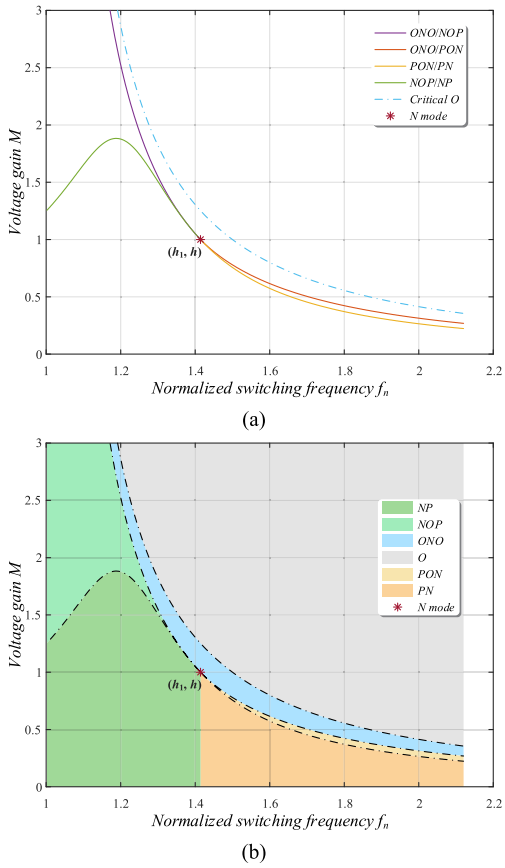

Fig. 6. (a) Typical mode boundaries and (b) distribution of *LCL* on the f_n–M plane.

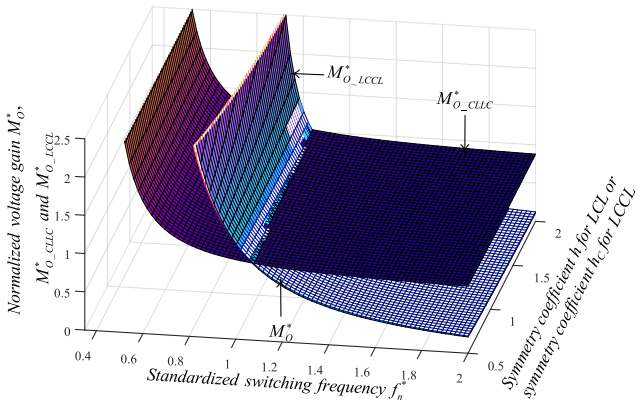

Fig. 7. Variations of M_O^*, $M_{O\_CLLC}^*$, and $M_{O\_LCCL}^*$ versus standardized switching frequency f_n^* and symmetry coefficient h (or h_C).

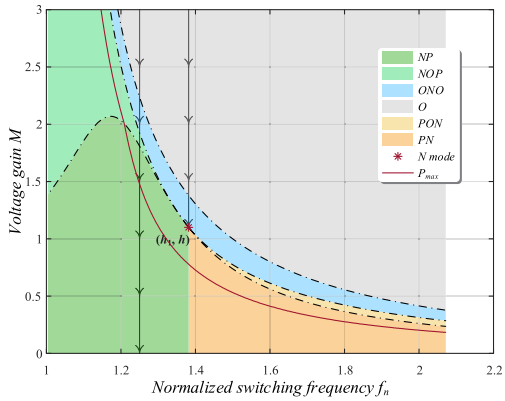

Fig. 8. Modes distribution and $P_{\max}$ at a certain frequency of *LCL* in the f_n–M plane.

To compare M_O, M_{O_CLLC}, and M_{O_LCCL} fairly, each of them is normalized according to their constant voltage gain (e.g., $f_n = h_1, M = h$ for *LCL*, $f_n = 1, M_{CLLC} = 1$ for *CLLC*, and $f_n = ((h_C k_C + h_C + 1)/(h_C k_C))^{1/2}, M_{LCCL} = h_C$ for *LCCL*, where h_C is the symmetry coefficient of S-type *LCCL* [14]). Consequently, M_O^*, $M_{O\_CLLC}^*$, and $M_{O\_LCCL}^*$ are provided in (18)–(20) as the normalized M_O, M_{O_CLLC}, and M_{O_LCCL} respectively, where f_n^* is the normalized f_n with respect to the respective constant voltage gain frequency (e.g., $f_n = h_1$ for *LCL*, $f_n = 1$ for *CLLC* and $f_n = ((h_C k_C + h_C + 1)/(h_C k_C))^{1/2}$ for *LCCL*).

$$\begin{cases} M_O^* = \frac{M_O}{h} \\ f_n^* = \frac{f_n}{h_1} \end{cases} \Rightarrow M_O^* = \frac{1}{h}\left(\sec\left(\frac{\pi}{2 f_n^* h_1}\right) - 1\right) \tag{18}$$

$$\begin{cases} M_{O\_CLLC}^* = \frac{M_{O\_CLLC}}{1} \\ f_n^* = \frac{f_n}{1} \Rightarrow \\ M_{O\_CLLC}^* = \frac{1}{k_L+1}\sec\left(\sqrt{\frac{k_L}{k_L+1}}\pi \Big/ (2 f_n^*)\right) \end{cases} \tag{19}$$

$$\begin{cases} M_{O\_LCCL}^* = \frac{M_{O\_LCCL}}{h_C} \\ f_n^* = \frac{f_n}{\sqrt{\frac{h_C k_C + h_C + 1}{h_C k_C}}} \Rightarrow \\ M_{O\_LCCL}^* = \frac{1}{h_C(k_C+1)}\left(\sec\left(\frac{\sqrt{\frac{k_C+1}{k_C}}\pi}{2 f_n^* \sqrt{\frac{h_C k_C + h_C + 1}{h_C k_C}}}\right) - 1\right). \end{cases} \tag{20}$$

The variations of M_O^*, $M_{O\_CLLC}^*$, and $M_{O\_LCCL}^*$ versus f_n^* and h (or h_C) are depicted in Fig. 7, where $h \equiv h_C$, $k = k_L = 0.2$ holds. Clearly, both *LCL* and *LCCL* offer superior capability to step-up voltage than *CLLC* when $f_n^* < 1$, and both *LCL* and *LCCL* possess stronger characteristics to step-down voltage compared to *CLLC* when $f_n^* > 1$. In addition, both the step-up and step-down voltage capabilities of *LCL* are slightly inferior to that of *LCCL*. Considering that *LCL* requires fewer resonant components than *LCCL*, *LCL* achieves a better balance between cost, complexity, and voltage regulation capability.

5) Power Transfer Characteristics: To comprehensively derive the power transfer characteristics of *LCL* resonant tank, the entire f_n–M plane (i.e., Fig. 8) is mapped into f_n-M-$P_{\text{out\_}n}$ three-dimensional space utilizing time-domain calculations, as

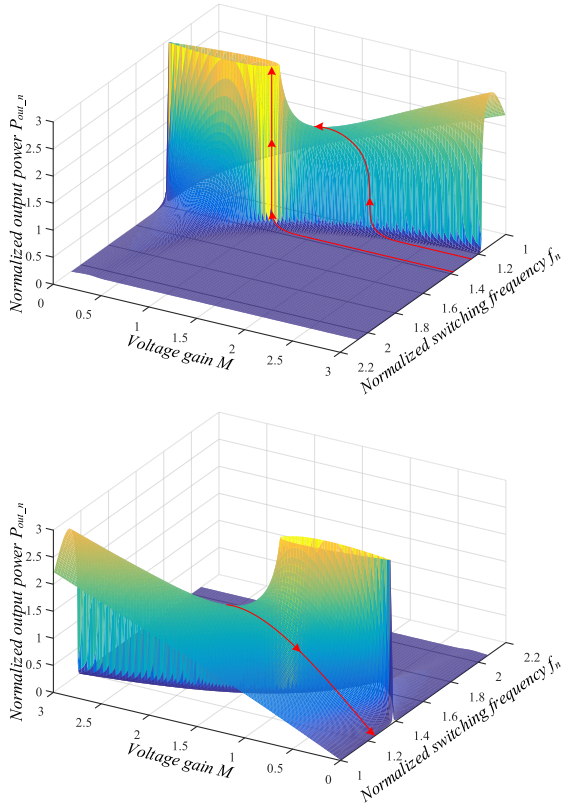

Fig. 9. Variations of $P_{\text{out\_}n}$ versus f_n and M.

illustrated in Fig. 9. It is not difficult to observe that for an *LCL* operating at a specific frequency (i.e., the arrow lines presented in Figs. 8 and 9), as the voltage gain M progressively decreases from a large value to 0, the operating mode of *LCL* goes through various modes in sequence, beginning with O mode and finally exhibiting an output short-circuit state (i.e., $M = 0$). During the process of M reduction, $P_{\text{out\_}n}$ first grows from 0 (i.e., O mode) to some peak $P_{\max}$ and subsequently drops to 0 (i.e., output short-circuit state) again. However, for an *LCL* operating at resonant frequency $f_n = h_1$, as M progressively decreases from a large value to h, the operating mode of the resonant tank

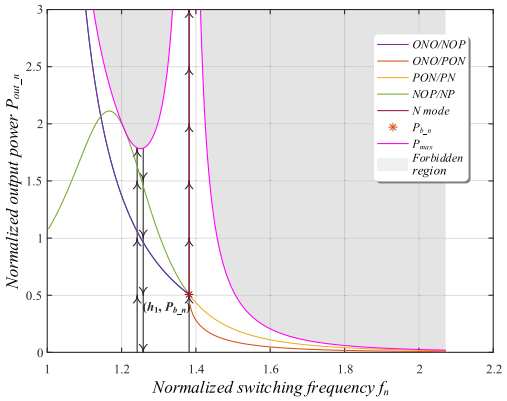

Fig. 10. Modes distribution and $P_{\max}$ at a certain frequency of *LCL* in the f_n–$P_{\text{out\_}n}$ plane.

TABLE IV
CONSTRAINTS FOR BOUNDARIES INTERSECTIONS

Intersection	Solving mode	Constraint
ONO/PON, ONO/NOP, PON/PN, NOP/NP	N	$m_{CTN}(\theta_{N0})$=-M=-h or $m_{CTN}(\theta_{P0})$=M=h

sequentially passes through O mode, ONO mode, and eventually behaves as N mode at $M = h$. As previously claimed N mode in (12), *LCL* operating at $f_n = h_1$ can maintain N mode providing that $I_{\text{out\_}n}I_{b\_n}$. Therefore, the relevant $P_{\text{out\_}n}$ for N mode is $P_{\text{out\_}n} = MI_{\text{out\_}n}hI_{b\_n}$, i.e., *LCL* operating in N mode can provide unlimited power. As M continues to decrease from h, the response of the resonant tank will oscillate and diverge, which should be avoided in practice.

Intended to obtain power transfer characteristics of *LCL* more visually, both Fig. 9 and relevant $P_{\max}$ at a certain frequency are projected to the f_n–$P_{\text{out\_}n}$ plane, as depicted in Fig. 10. Evidently, the variation of $P_{\text{out\_}n}$ is nonmonotonic as M decreases at a specific frequency (i.e., the arrow lines shown in Figs. 8 and 9), which means that the projection of Fig. 9 will cover the f_n–$P_{\text{out\_}n}$ plane twice. Therefore, Fig. 10 is further divided into the two subplots in Fig. 11, illustrating the variation of $P_{\text{out\_}n}$ monotonically increasing or decreasing with the decreases of M at a certain frequency respectively.

It is not difficult to notice that the mode boundaries (i.e., ONO/PON, PON/PN, ONO/NOP, and NOP/NP plotted in Fig. 8) intersect at (h_1, h) on the f_n–M plane. Likewise, those boundaries depicted in Fig. 10 also intersect at a special point P_{b_n} on the f_n–$P_{\text{out\_}n}$ plane, implying that this intersection of those boundaries is a special N mode. Accordingly, this special N mode can be derived by appending associated mode boundary constraints, which are provided in Table IV.

The load conditions (e.g., output current $I_{\text{out\_}n}$ and output power P_{b_n}) of the intersection are obtained in (21), which is precisely the same load condition of the critical N mode in (12).

$$\begin{cases} I_{\text{out\_}n} = \frac{2}{\pi h_1} = I_{b\_n} \\ P_{b\_n} = hI_{b\_n} = \frac{2h}{\pi h_1} \end{cases}. \tag{21}$$

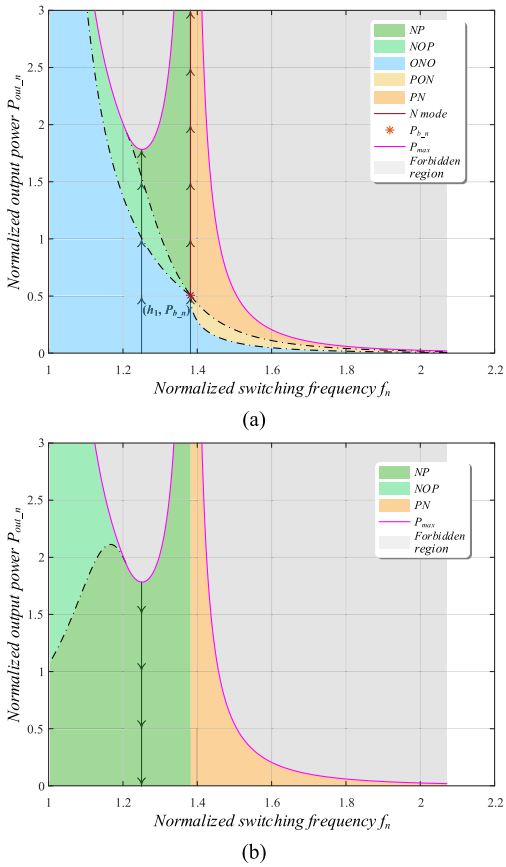

Fig. 11. Variation of $P_{\text{out\_}n}$ as M decreases at a certain frequency. (a) $P_{\text{out\_}n}$ increases monotonically. (b) $P_{\text{out\_}n}$ decreases monotonically.

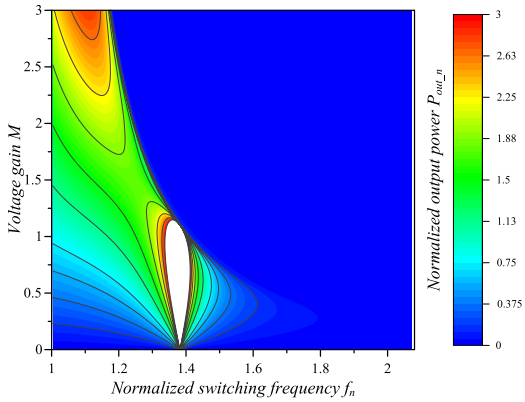

Fig. 12. Projection of constant power gain curves on the f_n–M plane.

Finally, to obtain the constant power gain curve of *LCL*, the constant $P_{\text{out\_}n}$ contours of Fig. 9 are projected to the f_n–M plane in Fig. 12. In a comprehensive analysis of Figs. 8–12, it is not difficult to notice that the constant power gain curves become nonmonotonic in BRR if $P_{\text{out\_}n}$ exceeds the minimum value of $P_{\max}$ in BRR. Therefore, in order to obtain monotonic constant power gain curves in practice, the designed maximum $P_{\text{out\_}n}$ should not exceed the minimum value of $P_{\max}$ in BRR.

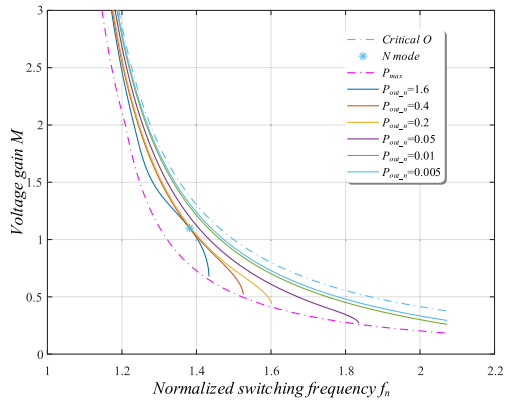

(a)

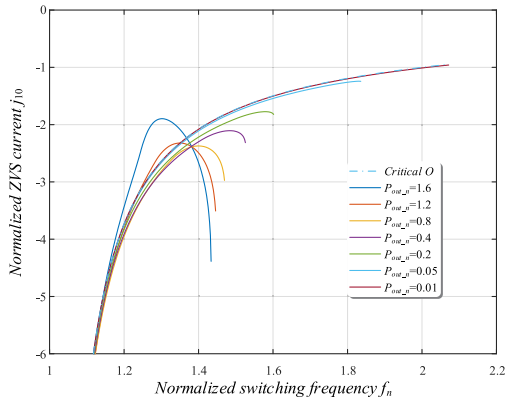

(b)

Fig. 13. Constant power gain curves under (a) different $P_{\text{out\_}n}$ and (b) corresponding ZVS current j_{10}.

In addition, the condition for the inverting side of *LCL* to achieve ZVS during forward operation is given as

$$|j_{10}|\, I_{\text{base}} t_{\text{dead}} \geq 2C_{oss}U_1 \Rightarrow |j_{10}|\, t_{\text{dead}} \geq 2C_{oss}Z_{\text{base}} \quad (22)$$

where j_{10} is the normalized i_1 at the beginning of the positive half-cycle, and C_{oss} denotes the output capacitor of corresponding switches.

The constant power gain curves of *LCL* for different $P_{\text{out\_}n}$ conditions and corresponding ZVS current j_{10} are accurately obtained through time-domain calculations, as illustrated in Fig. 13.

B. Reverse Operation

As for the reverse operation of *LCL* described in Fig. 14, the following definitions are provided in (23) and (24), where subscript *R* denotes the corresponding normalization bases of reverse operation.

$$\begin{aligned} &\omega_{\text{base\_}R} = (L_{se}C_T)^{-1/2} = 2\pi f_{\text{base\_}R}, \quad U_{\text{base\_}R} = nU_2 \\ &Z_{\text{base\_}R} = \sqrt{L_{se}/C_T} = \sqrt{h}Z_{\text{base}}, \quad I_{\text{base\_}R} = U_{\text{base\_}R}/Z_{\text{base\_}R} \end{aligned} \quad (23)$$

$$\begin{cases} h' = L_p/L_{se} = 1/h \\ f_r/f_{\text{base\_}R} = \sqrt{h+1} = h'_1 \end{cases}. \quad (24)$$

TABLE V
DESIGN SPECIFICATIONS

Parameters	Symbol	Value
Input voltage	U_1	400 V
Battery voltage range	$U_{2m} - U_{2M}$	250–450 V
Resonant frequency	f_r	100 kHz
Operating frequency range	$f_{s,\min}$ $f_{s,\max}$	75–150 kHz
Rated power	P_{rated}	1 kW

Apparently, only the parameter h' differs between the reverse and forward operations of *LCL*. Therefore, the corresponding modes analysis and power transfer characteristics of the reverse operation are similar to those of the forward operation and will not be repeated.

Besides, the requirement for the inverting side of *LCL* to achieve ZVS during reverse operation is specified in (25), where j_{20_R} is the normalized i_{2_R} at the beginning of the positive half-cycle.

$$\begin{aligned} &n\,|j_{20\_R}|\, I_{\text{base\_}R} t_{\text{dead}} \geq 2C_{oss}U_2 \\ &n\,|j_{20\_R}|\, {}^{nU_2}/_{Z_{\text{base\_}R}} t_{\text{dead}} \geq 2C_{oss}U_2 \\ &|j_{20\_R}|\, n^2 t_{\text{dead}} \geq 2C_{oss}Z_{\text{base\_}R}. \end{aligned} \quad (25)$$

IV. Design Considerations

For bidirectional EV charger applications, the wide voltage range of the battery presents a considerable challenge to the design optimization of the bidirectional *LCL* resonant tank. In this section, TDM is utilized to search for the optimal *LCL* parameters (L_p, C_T, h, n) to address the aforementioned challenge.

A 1 kW bidirectional *LCL* converter is implemented to demonstrate the proposed design method. All the design specifications are listed in Table V.

Considering the voltage and power ratings summarized in Table V, Sct3080al SiC MOSFET is chosen for both the primary and secondary full bridges. To achieve ZVS during bidirectional operations, the output capacitance C_{oss} of both primary and secondary switches should be determined first. Taking into account the voltage levels of the primary and secondary sides and the relevant datasheet of Sct3080al, the C_{oss} of primary and secondary switches are determined to be 125 pF and 150 pF, respectively. In addition, the dead band in this article is 100 ns as

$$\begin{cases} C_{oss1} = 125\,\text{pF} \\ C_{oss2} = 150\,\text{pF} \\ t_{\text{dead}} = 100\,\text{ns} \end{cases}. \quad (26)$$

To begin with, to ensure that *LCL* experiences N mode (constant voltage gain) at $f_s = f_r$ during bidirectional operations under rated load, the following two conditions should be satisfied: 1) the designed minimum switching frequency $f_{s,\min}$ should be limited within BRR; 2) considering the uncertainty of n, the voltage gain range of both forward-operating M_m–M_M and reverse-operating M_{Rm}–M_{RM} should consistently contain the constant voltage gain (i.e., h and h') during bidirectional operations. The corresponding derivations are described in (27)

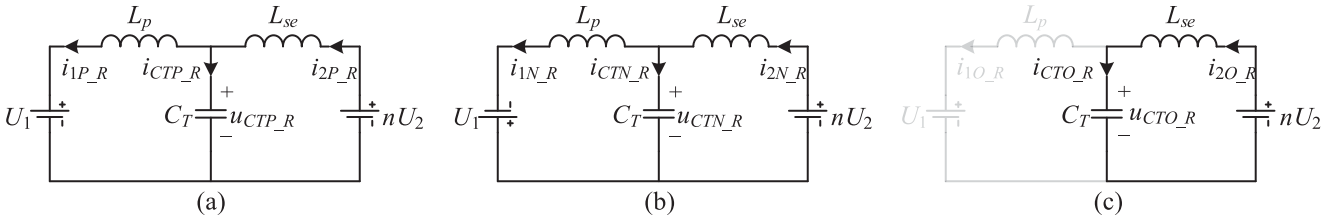

Fig. 14. Equivalent circuit of the *LCL* resonant tank in positive half-cycle for reverse operation. (a) P stage. (b) N stage. (c) O stage.

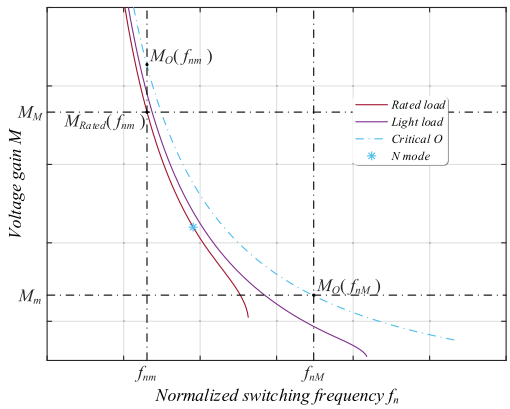

Fig. 15. Typical constant power gain curves of *LCL*.

and (28) respectively.

$$\begin{cases} h>0 \text{ and } \frac{f_{s,\min}}{f_{\text{base}}}>1 \\ h'>0 \text{ and } \frac{f_{s,\min}}{f_{\text{base\_}R}}>1 \\ f_r = h_1 f_{\text{base}} = h'_1 f_{\text{base\_}R} = 100\,\text{kHz} \end{cases}$$
$$\Rightarrow \begin{cases} \frac{3}{4}h_1>1 \\ \frac{3}{4}h'_1>1 \end{cases} \Rightarrow \frac{7}{9}<h<\frac{9}{7} \tag{27}$$

$$\begin{cases} M_m = \frac{nU_{2m}}{U_1} \le h \le M_M = \frac{nU_{2M}}{U_1} \\ M_{Rm} = \frac{1}{M_M} \le h' = \frac{1}{h} \le M_{RM} = \frac{1}{M_m} \end{cases}$$
$$\Rightarrow \frac{8}{9}h \le n \le \frac{8}{5}h. \tag{28}$$

In addition, several typical constant power gain curves of Fig. 12 are redrawn in Fig. 15, where M_{rated} indicates the gain curve of rated load for the design, M_O describes the gain curve of critical O mode under zero load, and f_{nM} and f_{nm} are the maximum and minimum normalized frequencies for forward operation, which are provided in (29). By observing the different constant power gain curves in Figs. 12 and 15, it is not difficult to conclude that boosting voltage for heavier load conditions is more difficult within BRR, while lowering voltage for lighter load conditions is more challenging within ARR, that is, for the qualified *LCL* parameters that meet the design requirements, which should be capable of achieving the required maximum voltage gain M_M (and M_{RM}) under rated load conditions and the designed minimum voltage gain M_m (and M_{Rm}) under the lightest load condition during bidirectional operations within the required frequency range.

$$\begin{cases} f_{nM} = \frac{f_{s,\max}}{f_{\text{base}}} = \frac{f_{s,\max}}{f_r/h_1} = \frac{3}{2}\sqrt{\frac{h+1}{h}} \\ f_{nm} = \frac{f_{s,\min}}{f_{\text{base}}} = \frac{f_{s,\min}}{f_r/h_1} = \frac{3}{4}\sqrt{\frac{h+1}{h}} \end{cases}. \tag{29}$$

The most extreme light-load condition of *LCL* is the critical O mode under zero-load conditions, which has the strongest capability to step-up voltage and the weakest capability to step-down voltage. Accordingly, the gain characteristic M_O of critical O mode is provided in (30). Consequently, for the *LCL* parameters satisfying the design specifications, it is not difficult to derive the following conditions in (31) and (32) for forward operation.

$$M_O = \sec\left(\frac{\pi}{2f_n}\right) - 1 \tag{30}$$

$$M_{\text{Rated}}(f_{nm}) \ge M_M \tag{31}$$

$$M_O(f_{nM}) \le M_m. \tag{32}$$

Unfortunately, M_{rated} does not have a closed-form solution and cannot be utilized for further analytical derivation. Considering that M_O of the critical O mode is described analytically in closed form and that *LCL* possesses the strongest capability of boosting voltage under critical O mode, (31) is compromised into (33) for further derivation. It is important to note that the following equation is a necessary but insufficient condition:

$$M_O(f_{nm}) \ge M_{\text{Rated}}(f_{nm}) \ge M_M \Rightarrow M_O(f_{nm}) \ge M_M. \tag{33}$$

Up to now, the conditions for forward operation have been obtained in (32) and (33), which are further reduced in (34) and (35), respectively.

$$\sec\left(\frac{\pi}{2f_{nM}}\right) - 1 \le M_m \tag{34}$$

$$\sec\left(\frac{\pi}{2f_{nm}}\right) - 1 \ge M_M. \tag{35}$$

Similarly, the constraints for reverse operation are provided in (36) and (37), where f_{RnM} and f_{Rnm} listed in (38) are the maximum and minimum normalized frequencies for reverse operation. Subsequently, (34)–(37) are further reduced to (39)–(42), shown at the bottom of the next page respectively.

$$\sec\left(\frac{\pi}{2f_{RnM}}\right) - 1 \le M_{Rm} \tag{36}$$

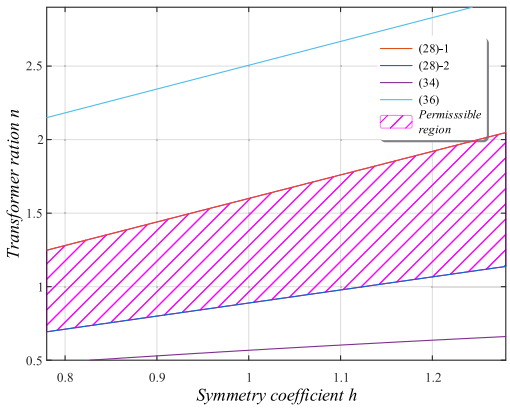

Fig. 16. Permissible region for parameters (n, h).

$$\sec\left(\frac{\pi}{2f_{Rnm}}\right)-1\geq M_{RM} \tag{37}$$

$$\begin{cases} f_{RnM}=\frac{f_{s,\max}}{f_{\text{base\_}R}}=\frac{f_{s,\max}}{f_r/h'_1}=\frac{3}{2}\sqrt{h+1} \\ f_{Rnm}=\frac{f_{s,\min}}{f_{\text{base\_}R}}=\frac{f_{s,\min}}{f_r/h'_1}=\frac{3}{4}\sqrt{h+1} \end{cases}. \tag{38}$$

Combining the derivation of (39)–(42), the possible range of transformer ratio n is determined in (43). As a result, all the conditions stemming from the design requirements are listed in (27)–(28) and (34)–(37). Finally, the possible (n, h) values that satisfy the design requirements are obtained by combining (27)–(28) and (34)–(37), and the relevant permissible region of (n, h) is illustrated in Fig. 16.

$$0.47913\leq n\leq 2.96834. \tag{43}$$

So far, only the specific resonant parameters (e.g., Z_{base}, L_p, C_T) associated with certain (n, h) remain unknown and will be obtained through the following iterations.

Step 1: Given n and the related allowable h according to (27)–(28) and (34)–(37).

Step 2: Utilizing the (n, h) picked in *Step* 1, the corresponding voltage gain ranges M_m–M_M and M_{Rm}–M_{RM} are specified for bidirectional operations. TDM is adopted to derive the normalized maximum power P_{nMt} that achieves M_M in forward operations and the normalized maximum power P_{nRMt} that is capable of realizing M_{RM} during reverse operation, both of which should be guaranteed within the required frequency range. Accordingly, the normalized rated power P_n is determined as the lesser of P_{nMt} and P_{nRMt}.

$$P_n=\min\left(P_{nMt},P_{nRMt}\right). \tag{44}$$

Step 3: The characteristic impedance Z_{base} is obtained from the rated power P_{rated} and normalized rated power P_n, and both the ZVS conditions of bidirectional operations are utilized to judge whether the full range of ZVS is achieved. The relevant derivations are provided in (45), where $|j_{10}|_{\min}$ and $|j_{20\_R}|_{\min}$ are the minimum ZVS current during bidirectional operations respectively.

If it is confirmed that the full range of ZVS is achieved, the current Step passes and Step 4 begins; otherwise, reduce P_n to enhance the ZVS capability and reiterate Step 3.

$$\begin{cases} Z_{\text{base}}=P_nU_1^2/P_{\text{rated}} \\ |j_{10}|_{\min}t_{\text{dead}}\geq 2C_{oss1}Z_{\text{base}} \\ |j_{20\_R}|_{\min}n^2t_{\text{dead}}\geq 2C_{oss2}\sqrt{h}Z_{\text{base}} \end{cases} \Rightarrow \begin{cases} \frac{|j_{10}|_{\min}}{P_n}\geq\frac{2C_{oss1}}{t_{\text{dead}}}\frac{U_1^2}{P_{\text{rated}}} \\ \frac{|j_{20\_R}|_{\min}}{P_n}\geq\frac{2C_{oss2}\sqrt{h}}{t_{\text{dead}}}\frac{U_1^2}{P_{\text{rated}}} \end{cases}. \tag{45}$$

Step 4: Check if all h associated with the given n have been iterated. If so, proceed to Step 5; otherwise, initiate iteration for another h associated with the given n.

Step 5: Check if all allowable n have been iterated. If yes, the iteration ends; otherwise, initiate iteration for another allowable n.

The flowchart of the iteration is illustrated in Fig. 17. After the completion of iterations, both P_n and Z_{base} for each (n, h) are yielded. Moreover, the specific resonant parameters associated

$$\begin{aligned} &\exists h\in\left(\tfrac{7}{9},\tfrac{9}{7}\right),\sec\left(\tfrac{\pi}{2f_{nM}}\right)-1\leq M_m\Rightarrow\tfrac{nU_{2m}}{U_1}\geq\min_{h\in\left(\frac{7}{9},\frac{9}{7}\right)}\left(\sec\left(\tfrac{\pi}{2f_{nM}}\right)-1\right)\Rightarrow\tfrac{nU_{2m}}{U_1}\geq\sec\left(\tfrac{\pi}{2f_{nM}}\right)-1\Big|_{h=\frac{7}{9}} \\ &\Rightarrow n\geq\tfrac{U_1}{U_{2m}}\left(\sec\left(\tfrac{\pi}{2f_{nM}}\right)-1\Big|_{h=\frac{7}{9}}\right)\Rightarrow n\geq\tfrac{1}{5}\left(8\sec\left(\tfrac{\sqrt{7}\pi}{12}\right)-8\right)\approx 0.47913 \end{aligned} \tag{39}$$

$$\exists h\in\left(\frac{7}{9},\frac{9}{7}\right),\sec\left(\frac{\pi}{2f_{nm}}\right)-1\geq M_M\Rightarrow\frac{nU_{2M}}{U_1}\leq\max_{h\in\left(\frac{7}{9},\frac{9}{7}\right)}\left(\sec\left(\frac{\pi}{2f_{nM}}\right)-1\right)\Rightarrow n>0 \tag{40}$$

$$\begin{aligned} &\exists h\in\left(\tfrac{7}{9},\tfrac{9}{7}\right),\sec\left(\tfrac{\pi}{2f_{RnM}}\right)-1\leq M_{Rm}\Rightarrow 1\Big/\tfrac{nU_{2M}}{U_1}\geq\min_{h\in\left(\frac{7}{9},\frac{9}{7}\right)}\left(\sec\left(\tfrac{\pi}{2f_{nM}}\right)-1\right)\Rightarrow\tfrac{U_1}{nU_{2M}}\geq\sec\left(\tfrac{\pi}{2f_{RnM}}\right)-1\Big|_{h=\frac{9}{7}} \\ &\Rightarrow n\leq\tfrac{U_1}{U_{2M}}\Big/\left(\sec\left(\tfrac{\pi}{2f_{RnM}}\right)-1\Big|_{h=\frac{9}{7}}\right)\Rightarrow n\leq 8\Big/\left(9\sec\left(\tfrac{\sqrt{7}\pi}{12}\right)-9\right)\approx 2.96834 \end{aligned} \tag{41}$$

$$\exists h\in\left(\frac{7}{9},\frac{9}{7}\right),\sec\left(\frac{\pi}{2f_{Rnm}}\right)-1\geq M_{RM}\Rightarrow 1\Big/\frac{nU_{2m}}{U_1}\leq\max_{h\in\left(\frac{7}{9},\frac{9}{7}\right)}\left(\sec\left(\frac{\pi}{2f_{Rnm}}\right)-1\right)\Rightarrow n>0 \tag{42}$$

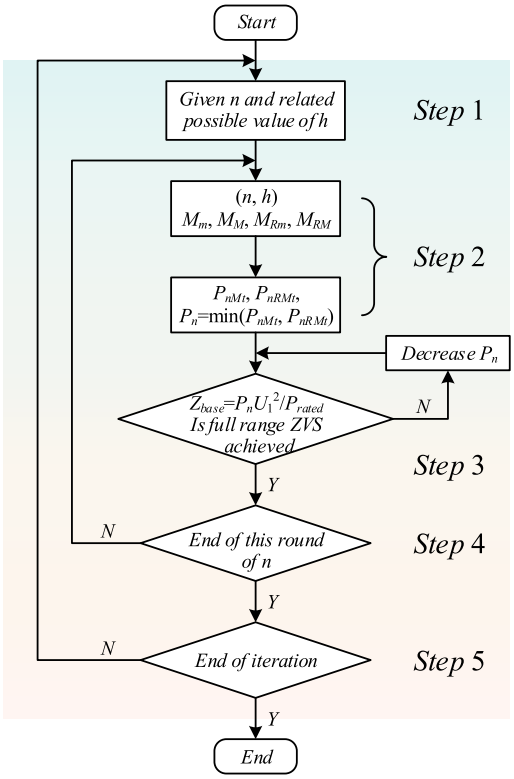

Fig. 17. Flowchart of the proposed iteration.

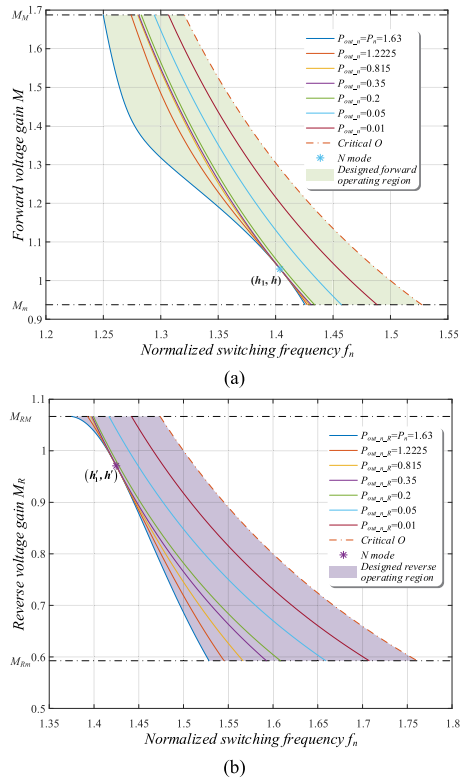

Fig. 18. Constant power gain curves of the optimized *LCL* for bidirectional operation. (a) Forward operation. (b) Reverse operation.

with certain qualified (n, h) are derived as follows:

$$\begin{cases} \omega_r = \sqrt{\frac{h+1}{h}}\frac{1}{\sqrt{L_pC_T}} \\ Z_{\text{base}} = \sqrt{\frac{L_p}{C_T}} \end{cases} \Rightarrow \begin{cases} L_p = \frac{Z_{\text{base}}}{\omega_r}\sqrt{\frac{1+h}{h}} \\ C_T = \sqrt{\frac{1+h}{h}}\Big/(Z_{\text{base}}\omega_r) \\ L_s = \frac{hL_p}{n^2} = \frac{hZ_{\text{base}}}{n^2\omega_r}\sqrt{\frac{1+h}{h}} \end{cases}. \tag{46}$$

For a certain eligible (n, h), the constant power gain curves of the related *LCL* during bidirectional operations are precisely obtained through time-domain calculations, as illustrated in Fig. 18, where $P_{\text{out\_}n\_R}$ is the normalized output power of reverse operation. Furthermore, for each operating point of desired load conditions, the corresponding normalized time-domain waveform of the positive half-cycle is also obtained, as depicted in Fig. 19, where θ_z is the zero-crossing moment of the inverting-side current j_1. Consequently, the associated charge Q_a for a given operating point is defined as the integral of the inverting-side current in the same direction as the inverting voltage during the positive half-cycle and the corresponding backflow charge Q_b is defined as the integral of the inverting-side current in the opposite direction as the inverting voltage during the positive half-cycle, as derived in (47) and (48), respectively.

$$Q_a = \int_{\frac{\theta_z}{\omega_{\text{base}}}}^{\frac{\pi}{\omega_{\text{base}} f_n}} i_1(t)dt = \frac{U_1}{Z_{\text{base}}}\frac{1}{\omega_{\text{base}}}\int_{\theta_z}^{\frac{\pi}{f_n}} j_1(\theta)d\omega_{\text{base}}t$$

$$= U_1\Big/\left(\sqrt{\frac{L_p}{C_T}}\right)\sqrt{L_pC_T}\int_{\theta_z}^{\frac{\pi}{f_n}} j_1(\theta)d\theta$$

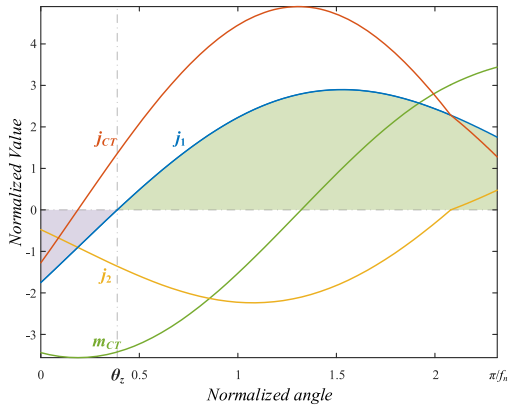

Fig. 19. Normalized time-domain waveforms of *LCL* during positive half-cycle.

$$= U_1C_T\int_{\theta_z}^{\frac{\pi}{f_n}} j_1(\theta)d\theta \tag{47}$$

$$Q_b = \int_0^{\frac{\theta_z}{\omega_{\text{base}}}} i_1(t)dt = \frac{U_1}{Z_{\text{base}}}\frac{1}{\omega_{\text{base}}}\int_0^{\theta_z} j_1(\theta)d\omega_{\text{base}}t$$

$$= U_1\Big/\left(\sqrt{\frac{L_p}{C_T}}\right)\sqrt{L_pC_T}\int_0^{\theta_z} j_1(\theta)d\theta$$

$$= U_1C_T\int_0^{\theta_z} j_1(\theta)d\theta. \tag{48}$$

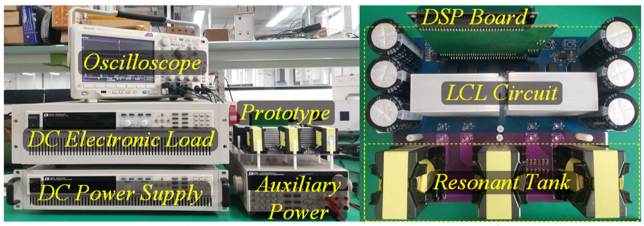

(a) (b)

Fig. 20. Experimental setup. (a) Experimental test platform. (b) *LCL* prototype.

Apparently, the power related to Q_b is the circulating reactive power. To describe the effective power for a certain operating point more intuitively, the corresponding effective charge Q_e is defined as the difference between the associated charge Q_a and the absolute value of the backflow charge Q_b, as derived in (49). Finally, the effective charge factor η is defined as the ratio of the effective charge Q_e to the associated charge Q_a in (50).

$$\begin{aligned} Q_e &= Q_a - |Q_b| = U_1 C_T \int_{\theta_z}^{\frac{\pi}{f_n}} j_1(\theta) d\theta - \left| U_1 C_T \int_0^{\theta_z} j_1(\theta) d\theta \right| \\ &= U_1 C_T \left(\int_{\theta_z}^{\frac{\pi}{f_n}} j_1(\theta) d\theta - \left| \int_0^{\theta_z} j_1(\theta) d\theta \right| \right) \end{aligned} \tag{49}$$

$$\begin{aligned} \eta &= \frac{Q_e}{Q_a} = \left(\int_{\theta_z}^{\frac{\pi}{f_n}} j_1(\theta) d\theta - \left| \int_0^{\theta_z} j_1(\theta) d\theta \right| \right) \Big/ \left(\int_{\theta_z}^{\frac{\pi}{f_n}} j_1(\theta) d\theta \right) \\ &= 1 - \left(\left| \int_0^{\theta_z} j_1(\theta) d\theta \right| \right) \Big/ \left(\int_{\theta_z}^{\frac{\pi}{f_n}} j_1(\theta) d\theta \right). \end{aligned} \tag{50}$$

Obviously, the larger the η is, the smaller the percentage of backflow charge (i.e., circulating reactive power) of the corresponding operating point. Accordingly, the value of η is 1 when the inverting side presents purely resistive (i.e., $\theta_z = 0$) and 0 when the converter is operating in zero-load O mode [i.e., $\theta_z = \pi/(2f_n)$]. Therefore, the effective charge factor η is adopted to evaluate the quality of the operating point. However, there are an infinite number of operating points for a certain eligible (n, h), as shown in Fig. 18. Considering that the rated-load condition is the most significant characteristic of the converter, the average of the effective charge factor η for all operating points on the rated-load gain curve is adopted to characterize the performance of corresponding design parameters, as derived in (51). Besides, since there are also reverse operating conditions, the effective charge factor η_R for reverse operation is also derived in (52), where θ_{zR} is the zero-crossing moment of the inverting-side current for reverse operation.

$$\bar{\eta} = \sum_{i=1}^{N} \eta_i \Big/ N \tag{51}$$

$$\eta_R = \frac{Q_{eR}}{Q_{aR}} = 1 - \left(\left| \int_0^{\theta_{zR}} j_{2\_R}(\theta) d\theta \right| \right) \Big/ \left(\int_{\theta_{zR}}^{\frac{\pi}{f_n}} j_{2\_R}(\theta) d\theta \right). \tag{52}$$

TABLE VI
ITERATION RESULTS

Permissible n	(n, h)	P_n	Z_{base}	$\bar{\eta}_B$
0.5	-	-	-	-
0.6	-	-	-	-
0.7	(0.7, 0.78)	0.52	83.2	0.7043
0.8	(0.8, 0.78)	0.63	100.8	0.7356
0.9	(0.9, 0.78)	0.76	121.6	0.7573
1.0	(1.0, 0.78)	0.95	152	0.7960
1.1	(1.1, 0.79)	1.2	192	0.8395
1.2	(1.2, 0.85)	1.31	209.6	0.8440
1.3	(1.3, 0.91)	1.42	227.2	0.8474
1.4	(1.4, 0.97)	1.53	244.8	0.8496
1.5	**(1.5, 1.03)**	**1.63**	**260.8**	**0.8498**
1.6	(1.6, 1.09)	1.73	276.8	0.8482
1.7	(1.7, 1.15)	1.83	292.8	0.8478
1.8	(1.8, 1.20)	1.97	315.2	0.8489
1.9	(1.9, 1.26)	2.08	332.8	0.8488
2.0	(2.0, 1.28)	2.12	339.2	0.8317
2.1	-	-	-	-
…	-	-	-	-
2.9	-	-	-	-

Similarly, the average effective charge factor $\bar{\eta}_R$ of all operating points on the rated-load gain curve during reverse operation is derived in (53). Considering that the characteristics of both forward and reverse operations are equally weighted for *LCL*, the bidirectional average effective charge factor $\bar{\eta}_B$ is defined as the average of $\bar{\eta}$ and $\bar{\eta}_R$ in (54), which is utilized to evaluate the performance of various eligible combinations of (n, h). In other words, the iteration result with the maximum $\bar{\eta}_B$ is selected as the optimal design. The iteration results with the maximum $\bar{\eta}_B$ of each allowable n are presented in Table VI.

$$\bar{\eta}_R = \sum_{i_R=1}^{N_R} \eta_{iR} \Big/ N_R \tag{53}$$

$$\bar{\eta}_B = (\bar{\eta}_R + \bar{\eta})/2. \tag{54}$$

According to Table VI, the associated permissible h of n = 0.5–0.6 and 2.1–2.9 is a null set. By comparing the bidirectional average effective charge factor $\bar{\eta}_B$ of various iterations, the optimal design parameters are determined in (55). In addition, the constant power gain curves of the optimal *LCL* during bidirectional operations are accurately obtained through time-domain calculations, as depicted in Fig. 18.

$$\begin{cases} n = 1.5 \\ h = 1.03 \\ Z_{\text{base}} = 260.8\ \Omega \\ f_r = 100\,\text{kHz} \end{cases} \Rightarrow \begin{cases} L_p = 582.716\ \mu\text{H} \\ C_T = 8.567\ \text{nF} \\ L_s = 266.7545\ \mu\text{H} \end{cases}. \tag{55}$$

V. EXPERIMENTAL RESULTS

To verify the correctness of the theoretical analysis and the effectiveness of the proposed parameters optimization method, an *LCL* prototype was implemented with parameters provided in (55) and the relevant specifications are enumerated in Table V. In addition, the key circuit component values are recapitulated in Table VII and the experimental setup is given in Fig. 20.

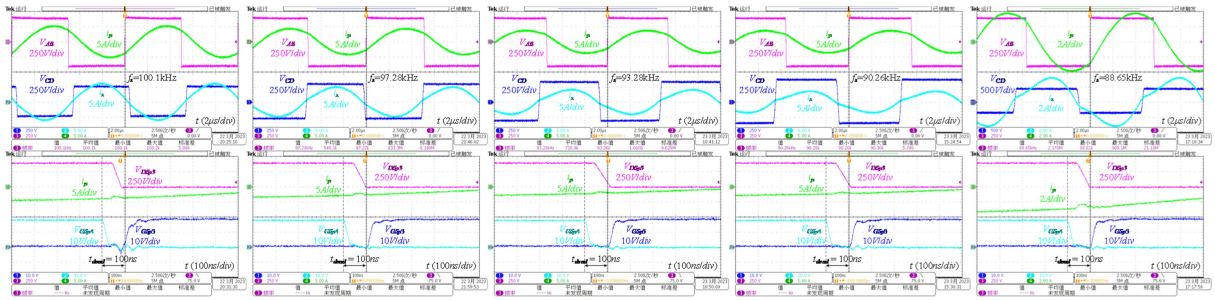

(a) (b) (c) (d) (e)

Fig. 21. Experimental waveforms of the prototype during forward operation under 1 kW load condition. (a) $U_1 = 400$ V, $U_2 = 250$ V. (b) $U_1 = 400$ V, $U_2 = 300$ V. (c) $U_1 = 400$ V, $U_2 = 350$ V. (d) $U_1 = 400$ V, $U_2 = 400$ V. (e) $U_1 = 400$ V, $U_2 = 450$ V.

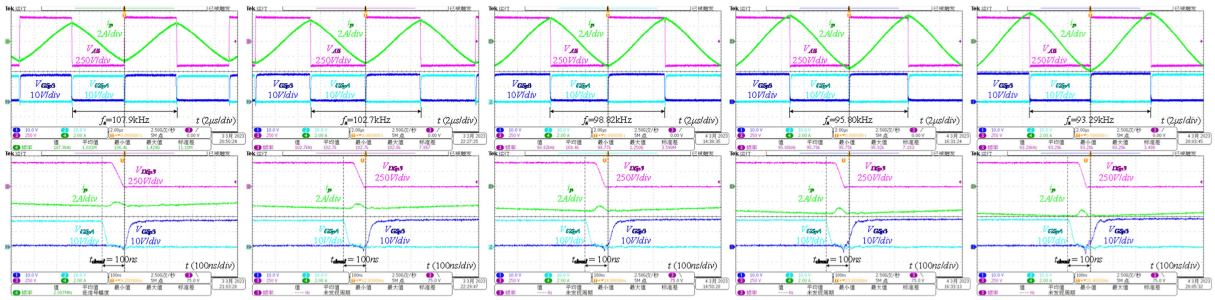

(a) (b) (c) (d) (e)

Fig. 22. Experimental waveforms of the prototype during forward operation under zero-load O mode. (a) $U_1 = 400$ V, $U_2 = 250$ V. (b) $U_1 = 400$ V, $U_2 = 300$ V. (c) $U_1 = 400$ V, $U_2 = 350$ V. (d) $U_1 = 400$ V, $U_2 = 400$ V. (e) $U_1 = 400$ V, $U_2 = 450$ V.

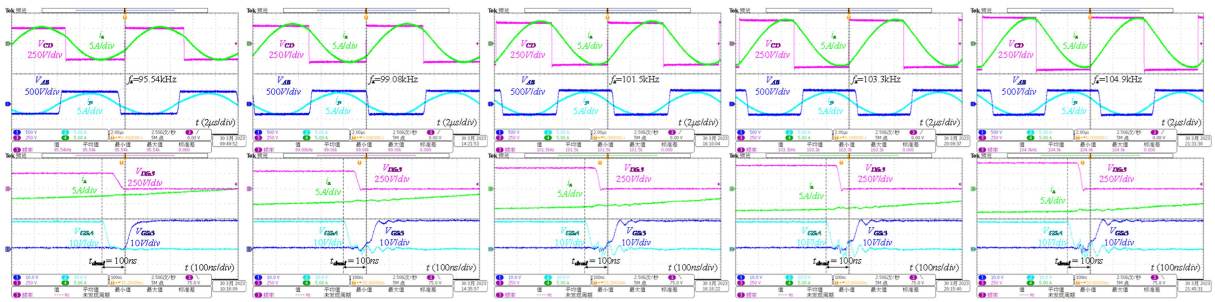

(a) (b) (c) (d) (e)

Fig. 23. Experimental waveforms of the prototype during reverse operation under 1 kW load condition. (a) $U_2 = 250$ V, $U_1 = 400$ V. (b) $U_2 = 300$ V, $U_1 = 400$ V. (c) $U_2 = 350$ V, $U_1 = 400$ V. (d) $U_2 = 400$ V, $U_1 = 400$ V. (e) $U_2 = 450$ V, $U_1 = 400$ V.

TABLE VII
KEY DESIGN PARAMETERS

Components	Parameter/Part#
Primary voltage U_1	400 V
Secondary voltage U_2	250–450 V
Primary resonant inductance L_p	582.716 μH
Parallel resonant capacitance C_T	8.567 nF
Secondary resonant inductance L_s	266.7545 μH
Turns ratio n	1.5
Resonant frequency f_r	100 kHz
Switching frequency f_s	75–150 kHz
Rated power	1 kW
MOSFETs	ROHM SCT3080AL

A. *Forward Operation*

Fig. 21 provides the detailed experimental waveforms of the prototype during forward operation at several typical voltage gains and constant 1 kW load conditions. It is not difficult to notice that the drain–source voltage V_{DSp3} can always drop to zero before S_{p3} turns ON, which is exactly the indication that ZVS for S_{p3} has been achieved. Similar waveforms implementing ZVS for forward operation are shown in Fig. 22, in which the load conditions are zero-load O mode. Therefore, the optimized *LCL* parameters derived by iteration are undoubtedly capable of offering the required voltage gain and guaranteeing

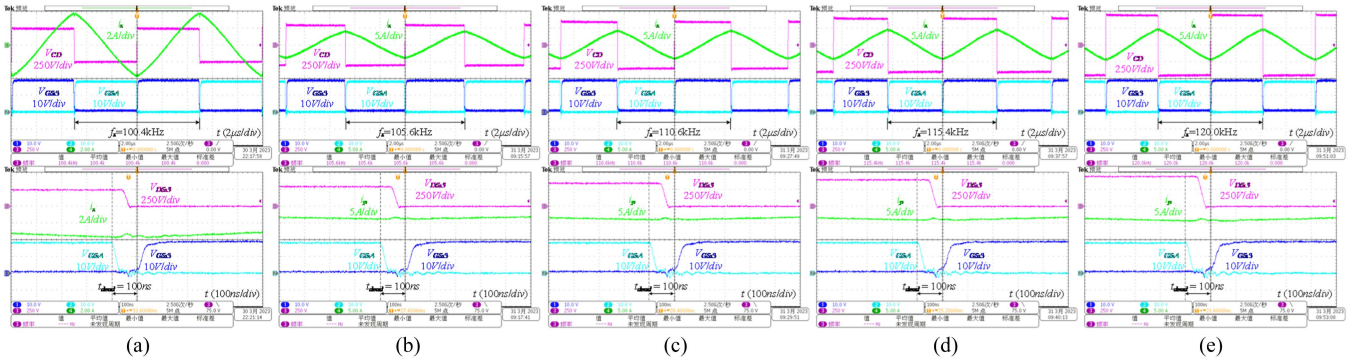

Fig. 24. Experimental waveforms of the prototype during reverse operation under zero-load O mode. (a) $U_2 = 250$ V, $U_1 = 400$ V. (b) $U_2 = 300$ V, $U_1 = 400$ V. (c) $U_2 = 350$ V, $U_1 = 400$ V. (d) $U_2 = 400$ V, $U_1 = 400$ V. (e) $U_2 = 450$ V, $U_1 = 400$ V.

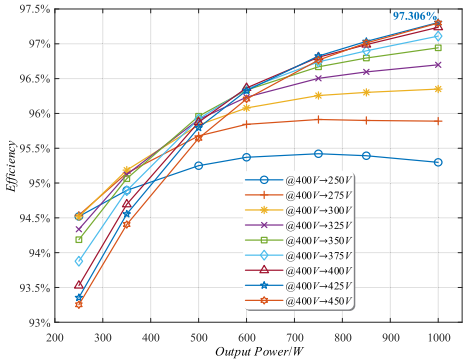

Fig. 25. Measured efficiency curves during forward operation.

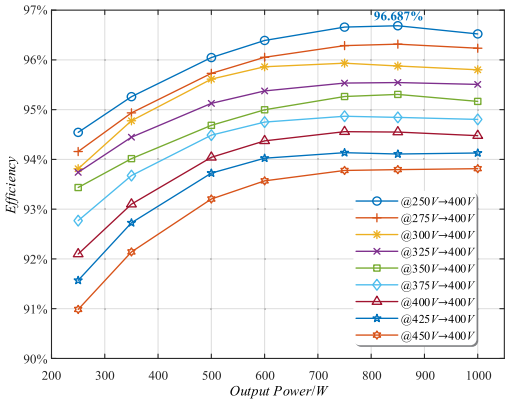

Fig. 26. Measured efficiency curves during reverse operation.

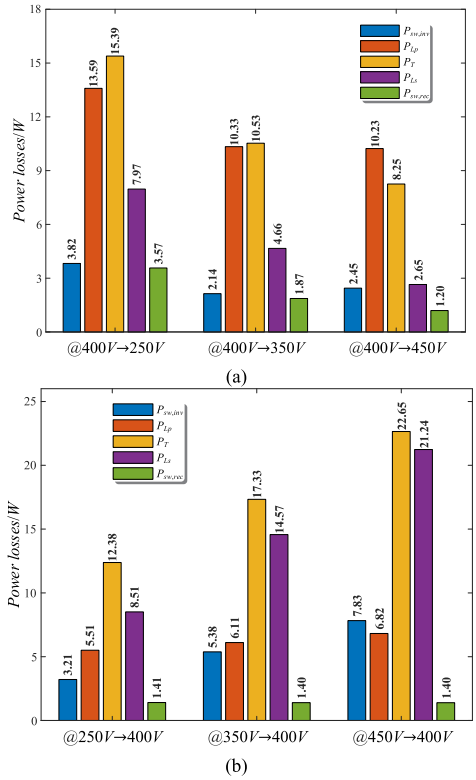

Fig. 27. Estimated loss breakdown of the prototype at typical voltages and 1 kW load condition during (a) forward mode and (b) reverse mode.

the achievement of ZVS under desired load conditions during forward operation.

B. Reverse Operation

Fig. 23 presents the detailed experimental waveforms of the prototype during reverse operation at several typical voltage gains and constant 1 kW load conditions. Clearly, ZVS for switch S_{s3} is achieved. Similar waveforms achieving ZVS for reverse operation are also listed in Fig. 24, in which the load conditions are zero-load O mode. Consequently, the optimized *LCL* parameters derived by iteration can provide the required voltage gain and guarantee the achievement of ZVS under required load conditions during reverse operation.

C. Efficiency Analysis

Figs. 25 and 26 present the measured efficiency curves of the *LCL* prototype during bidirectional operations under different load conditions. The peak efficiency of 97.306% is achieved at rated load conditions when $U_1 = 400$ V, $U_2 = 425$ V during forward operation. Owning to the achievement of the full range of ZVS with reduced reactive power, the efficiency of over 91% is maintained even under light-load conditions.

TABLE VIII
PERFORMANCE COMPARISONS OF THE PROPOSED *LCL* WITH EXISTING WORKS

Topology	Modulation Strategy	Switching Frequency	Analysis accuracy	Rated Power	Power Range*	Gain Range	Peak Efficiency	Efficiency at Full Load
SRC[32]	PFM and PWM	40−80 kHz	★	6 kW	0%–100%	2.0 ×	93%	85%−90%
LLC[33]	PWM and PS	100 kHz	★	1 kW	0%–100%	2.0 ×	96.5%	93.5%−96%
DAB[6]	PWM and PS	500 kHz	★★★	3.3 kW	Only 100%	1.5 ×	98%	90.5%−98%
LCL-DAB[27]	DPS	50 kHz	★	1 kW	Only 100%	2.0 ×	95.3%	93.1%−95.3%
LCLL[34]	PFM	65−120 kHz	★	1 kW	Only 100%	1.5 ×	95.94%	90.4%−95.94%
CLLC[12]	PFM	50−200 kHz	★★★	1 kW	50%–100%	1.8 ×	98.91%	97%−98.4%
CLTC[13]	PFM	45−160 kHz	★	5 kW	0%–100%	1.38 ×	97.1%	93.7%−95.9%
CDT-*LC*[35]	PFM	65−135 kHz	★★★	2.5 kW	0%–100%	1.58 ×	97%	93.2%−96.1%
LCCL[14]	PFM	88−117.9 kHz	★★★	1 kW	0%–100%	1.8 ×	97.357%	93.25%−97.35%
This work	**PFM**	**88.7−120 kHz**	★★★	**1 kW**	**0%–100%**	**1.8 ×**	**97.306%**	**93.81%−97.306%**

*Power range that both the full range of ZVS and the designed voltage gain are achieved.
"★" represents the unit of quantization, where ★ denotes the less accurate analytical approach, i.e., FHA, and ★★★ indicates the analysis method with excellent precision, i.e., TDM adopted in this article for resonant topology and piecewise linear method for DAB.

For the proposed *LCL* resonant converter, due to the achievement of full-range soft switching (i.e., ZVS for inverting-side switches and ZCS for rectifier switches) and synchronous rectification refer to [36], its power losses mainly include the following three parts: 1) inverting-side (i.e., primary side for forward mode and a secondary side for reverse mode) switch losses $P_{\mathrm{sw,inv}}$, including turn-OFF loss $P_{\mathrm{off,inv}}$ and conduction loss $P_{\mathrm{con,inv}}$; 2) rectifier side (i.e., secondary side for forward mode and primary side for reverse mode) switch losses $P_{\mathrm{sw,rec}}$, i.e., only conduction loss $P_{\mathrm{con,rec}}$; 3) magnetic losses, including transformer losses P_T, inductor losses P_{Lp}, and inductor losses P_{Ls}. Specifically, P_T, P_{Lp}, and P_{Ls} can further be subdivided into corresponding magnetic core loss and copper loss.

Accordingly, the estimated loss breakdown (i.e., $P_{\mathrm{sw,inv}}$, P_{Lp}, P_T, P_{Ls}, and $P_{\mathrm{sw,rec}}$) of the prototype at typical voltage gains and 1 kW load condition during bidirectional operation are derived in Fig. 27. Clearly, thanks to the achievement of full-range soft switching and the excellent device characteristics of SiC MOSFET, the estimated switch losses are consistently small. Especially, the rectifier side losses $P_{\mathrm{sw,rec}}$ after synchronous rectification is performed. Moreover, it is found that magnetic losses (i.e., P_{Lp}, P_T, and P_{Ls}) are the dominant part of the losses, which implies that there is still much potential for the optimization of the relevant magnetic components (i.e., L_p, T, and L_s), and the conversion efficiency of the prototype can further be improved in the future by optimizing the design of the magnetic components. Besides, the inductor losses of the inverting side are consistently larger than those of the rectifier side, and a similar scenario can also be observed for the switch losses. This is due to the presence of circulating reactive energy on the inverting-side resonant tank even after optimization, which results in extra losses of switches and magnetic components on the inverting side. On the other hand, it is exactly the reactive power on the inverting side that provides the proposed *LCL* with a wide range of voltage regulation capability.

D. Performance Comparisons

To comprehensively demonstrate the potential benefits of the proposed *LCL*, the performance comparison of *LCL* with existing works for bidirectional OBC applications is summarized in Table VIII. It is well known that neither SRC nor *LLC* can provide a bidirectional wide voltage gain range if only PFM is adopted. As a result, both SRC [32] and *LLC* [33] utilize additional modulation strategies (e.g., PWM and PS) to handle the requirement for a wide voltage gain range, which inevitably increases the complexity of the control implementation. As for DAB [6] and *LCL*-type DAB [27], even with the introduction of more sophisticated multiple PS modulation strategies (e.g., EPS, DPS, and TPS), they still suffer from loss of ZVS when operating over the full power range (0%–100%). Besides, excessive reactive power still exists for DAB operating under OBC applications. Therefore, the efficiency performance of DAB [6] and *LCL*-type DAB [27] is to remain inferior to that of the proposed *LCL*. Compared to the resonant tank configuration (e.g., *CLLC* [12], *CLTC* [13], *LCCL* [14], *LCLL* [34], and CDT-*LC* [35]) specifically optimized for bidirectional wide voltage gain applications adopting only PFM, both the proposed *LCL* and *LCCL* [14] are capable of realizing the design voltage gain with the narrowest frequency range. Admittedly, the overall efficiency performance of this work is slightly inferior to that of *CLLC* [12] since the *CLLC* is designed to realize a power range of 50%–100%, while the *LCL* of this work is compromised accordingly to achieve the entire power range of 0%–100%. Obviously, the proposed *LCL* requires fewer resonant components to provide superior performances similar to that of *LCCL* [14] under bidirectional OBC applications. Therefore, the proposed *LCL* provides a better tradeoff between cost, voltage regulation capability, ZVS, and efficiency.

VI. CONCLUSION

The *LCL* resonant tank adopting PFM is optimized for bidirectional OBC applications utilizing TDM in this article. The basic operating principles of *LCL* are reviewed and presented first. Then TDM is utilized to characterize the *LCL* resonant tank during bidirectional operations. With the accurate findings of TDM, an *LCL* resonant parameters optimization method is proposed to address the wide voltage range of battery charger application, which is capable of providing the required wide voltage gain and guaranteeing the achievement of ZVS with

reduced reactive power under desired load conditions during bidirectional operations. Finally, a 1-kW *LCL* prototype with an optimized resonant tank was constructed. The revealed experimental results confirmed the correctness of the TDM theoretical analysis and the effectiveness of the proposed parameters optimization method. Moreover, the superior performances of the *LCL* resonant tank over the entire power range (0%–100%) were well proven. Specifically, the optimized *LCL* prototype achieves the designed 1.8× voltage gain within a narrow switching frequency range of 88.7–120 kHz, with a measured peak efficiency of 97.306%.

REFERENCES

[1] Porsche, *Porsche Taycan*, 2022. [Online]. Available: https://www.porsche.com/USA/models/taycan/taycan-models/

[2] A. Khaligh and M. D'Antonio, "Global trends in high-power on-board chargers for electric vehicles," *IEEE Trans. Veh. Technol.*, vol. 68, no. 4, pp. 3306–3324, Apr. 2019.

[3] Z. Zhang, C. Liu, M. Wang, Y. Si, Y. Liu, and Q. Lei, "High-efficiency high-power-density CLLC resonant converter with low-stray-capacitance and well-heat-dissipated planar transformer for EV on-board charger," *IEEE Trans. Power Electron.*, vol. 35, no. 10, pp. 10831–10851, Oct. 2020.

[4] P. He, A. Mallik, A. Sankar, and A. Khaligh, "Design of a 1-MHz high-efficiency high-power-density bidirectional GaN-based CLLC converter for electric vehicles," *IEEE Trans. Veh. Technol.*, vol. 68, no. 1, pp. 213–223, Jan. 2019.

[5] N. Shafiei, M. Ordonez, M. Craciun, C. Botting, and M. Edington, "Burst mode elimination in high-power LLC resonant battery charger for electric vehicles," *IEEE Trans. Power Electron.*, vol. 31, no. 2, pp. 1173–1188, Feb. 2016.

[6] Y. Park, S. Chakraborty, and A. Khaligh, "DAB converter for EV onboard chargers using bare-die SiC MOSFETs and leakage-integrated planar transformer," *IEEE Trans. Transp. Electrific.*, vol. 8, no. 1, pp. 209–224, Mar. 2022.

[7] H. Xu, Z. Yin, Y. Zhao, and Y. Huang, "Accurate design of high-efficiency LLC resonant converter with wide output voltage," *IEEE Access*, vol. 5, pp. 26653–26665, 2017.

[8] X. Fang, H. Hu, Z. J. Shen, and I. Batarseh, "Operation mode analysis and peak gain approximation of the LLC resonant converter," *IEEE Trans. Power Electron.*, vol. 27, no. 4, pp. 1985–1995, Apr. 2012.

[9] F. Musavi, M. Craciun, D. S. Gautam, W. Eberle, and W. G. Dunford, "An LLC resonant DC–DC converter for wide output voltage range battery charging applications," *IEEE Trans. Power Electron.*, vol. 28, no. 12, pp. 5437–5445, Dec. 2013.

[10] C. Bai, B. Han, B.-H. Kwon, and M. Kim, "Highly efficient bidirectional series-resonant DC/DC converter over wide range of battery voltages," *IEEE Trans. Power Electron.*, vol. 35, no. 4, pp. 3636–3650, Apr. 2020.

[11] W. Chen, P. Rong, and Z. Lu, "Snubberless bidirectional DC–DC converter with new CLLC resonant tank featuring minimized switching loss," *IEEE Trans. Ind. Electron.*, vol. 57, no. 9, pp. 3075–3086, Sep. 2010.

[12] L. Zhao, Y. Pei, L. Wang, L. Pei, W. Cao, and Y. Gan, "Design methodology of bidirectional resonant CLLC charger for wide voltage range based on parameter equivalent and time domain model," *IEEE Trans. Power Electron.*, vol. 37, no. 10, pp. 12041–12064, Oct. 2022.

[13] C.-S. Wang, S.-H. Zhang, Y.-F. Wang, B. Chen, and J.-H. Liu, "A 5-kW isolated high voltage conversion ratio bidirectional CLTC resonant DC–DC converter with wide gain range and high efficiency," *IEEE Trans. Power Electron.*, vol. 34, no. 1, pp. 340–355, Jan. 2019.

[14] L. Zhao, Y. Pei, L. Wang, L. Pei, W. Cao, and Y. Gan, "Analysis and design of LCCL resonant converter based on time-domain model for bidirectional onboard charger applications," *IEEE Trans. Power Electron.*, vol. 38, no. 8, pp. 9852–9871, Aug. 2023.

[15] Y. Yan, H. Bai, A. Foote, and W. Wang, "Securing full-power-range zero-voltage switching in both steady-state and transient operations for a dual-active-bridge-based bidirectional electric vehicle charger," *IEEE Trans. Power Electron.*, vol. 35, no. 7, pp. 7506–7519, Jul. 2020.

[16] K. Siebke and R. Mallwitz, "Comparison of a dual active bridge and CLLC converter for on-board vehicle chargers using GaN and time domain modeling method," in *Proc. IEEE Energy Convers. Congr. Expo.*, 2020, pp. 1210–1216.

[17] M. Yaqoob, K. H. Loo, and Y. M. Lai, "Extension of soft-switching region of dual-active-bridge converter by a tunable resonant tank," *IEEE Trans. Power Electron.*, vol. 32, no. 12, pp. 9093–9104, Dec. 2017.

[18] M. Jafari, Z. Malekjamshidi, and J. G. Zhu, "Analysis of operation modes and limitations of dual active bridge phase shift converter," in *Proc. IEEE 11th Int. Conf. Power Electron. Drive Syst.*, 2015, pp. 393–398.

[19] G. Xu, D. Sha, J. Zhang, and X. Liao, "Unified boundary trapezoidal modulation control utilizing fixed duty cycle compensation and magnetizing current design for dual active bridge DC–DC converter," *IEEE Trans. Power Electron.*, vol. 32, no. 3, pp. 2243–2252, Mar. 2017.

[20] B. Zhao, Q. Song, W. Liu, and Y. Sun, "Overview of dual-active-bridge isolated bidirectional DC–DC converter for high-frequency-link power-conversion system," *IEEE Trans. Power Electron.*, vol. 29, no. 8, pp. 4091–4106, Aug. 2014.

[21] B. Zhao, Q. Yu, and W. Sun, "Extended-phase-shift control of isolated bidirectional DC–DC converter for power distribution in microgrid," *IEEE Trans. Power Electron.*, vol. 27, no. 11, pp. 4667–4680, Nov. 2012.

[22] H. Shi, H. Wen, J. Chen, Y. Hu, L. Jiang, and G. Chen, "Minimum-reactive-power scheme of dual-active-bridge DC–DC converter with three-level modulated phase-shift control," *IEEE Trans. Ind. Appl.*, vol. 53, no. 6, pp. 5573–5586, Nov./Dec. 2017.

[23] J. Hiltunen, V. Väisänen, R. Juntunen, and P. Silventoinen, "Variable-frequency phase shift modulation of a dual active bridge converter," *IEEE Trans. Power Electron.*, vol. 30, no. 12, pp. 7138–7148, Dec. 2015.

[24] M. Yaqoob, K. H. Loo, and Y. M. Lai, "A Four-degrees-of-freedom modulation strategy for dual-active-bridge series-resonant converter designed for total loss minimization," *IEEE Trans. Power Electron.*, vol. 34, no. 2, pp. 1065–1081, Feb. 2019.

[25] Q. Huang, K. Shi, X. Jia, C. Hu, and D. Xu, "A bi-directional resonant DC/DC converter with frequency tracking control," in *Proc. IEEE Energy Convers. Congr. Expo.*, 2014, pp. 4748–4754.

[26] R. P. Twiname, D. J. Thrimawithana, U. K. Madawala, and C. A. Baguley, "A new resonant bidirectional DC–DC converter topology," *IEEE Trans. Power Electron.*, vol. 29, no. 9, pp. 4733–4740, Sep. 2014.

[27] Z. Guo and M. Li, "An optimized DPS control strategy for LCL resonant dual active bridge converter for wide voltage conversion ratio," *IEEE J. Emerg. Sel. Topics Ind. Electron.*, vol. 2, no. 4, pp. 501–512, Oct. 2021.

[28] Z. Guo, M. Li, and X. Han, "Triple-phase shift modulation scheme of DAB converter with LCL resonant tank," *IEEE Trans. Transp. Electrific.*, vol. 8, no. 2, pp. 1734–1747, Jun. 2022.

[29] M. Li, X. Li, D. Yu, Y. Leng, and C. Zhang, "Perturbation observation method-based optimization seeking control of soft-switching and no backflow power for LCL resonant-type dual active bridge DC–DC converters," *IEEE Trans. Ind. Electron.*, vol. 70, no. 8, pp. 7810–7820, Aug. 2023.

[30] S. Mukherjee, J. M. Ruiz, and P. Barbosa, "A high power density wide range DC–DC converter for universal electric vehicle charging," *IEEE Trans. Power Electron.*, vol. 38, no. 2, pp. 1998–2012, Feb. 2023.

[31] Z. Lv, X. Yan, Y. Fang, and L. Sun, "Mode analysis and optimum design of bidirectional CLLC resonant converter for high-frequency isolation of DC distribution systems," in *Proc. IEEE Energy Convers. Congr. Expo.*, 2015, pp. 1513–1520.

[32] F. M. Ibanez, J. M. Echeverria, J. Vadillo, and L. Fontan, "A step-up bidirectional series resonant DC/DC converter using a continuous current mode," *IEEE Trans. Power Electron.*, vol. 30, no. 3, pp. 1393–1402, Mar. 2015.

[33] T. Jiang, J. Zhang, X. Wu, K. Sheng, and Y. Wang, "A bidirectional three-level LLC resonant converter with PWAM control," *IEEE Trans. Power Electron.*, vol. 31, no. 3, pp. 2213–2225, Mar. 2016.

[34] Y. Zhang, D. Zhang, J. Li, and H. Zhu, "Bidirectional LCLL resonant converter with wide output voltage range," *IEEE Trans. Power Electron.*, vol. 35, no. 11, pp. 11813–11826, Nov. 2020.

[35] B. Chen, P. Wang, Y.-F. Wang, S.-H. Zhang, L. Yang, and R.-L. Ji, "A bidirectional CDT-LC resonant DC–DC converter with a wide voltage range," *IEEE Trans. Ind. Electron.*, vol. 67, no. 3, pp. 2009–2020, Mar. 2020.

[36] L. Pei et al., "A time-domain-model-based digital synchronous rectification algorithm for CLLC resonant converters utilizing a hybrid modulation," *IEEE Trans. Power Electron.*, vol. 37, no. 3, pp. 2815–2829, Mar. 2022.

Lie Zhao (Member, IEEE) was born in Shaanxi, China, in 1996. He received the B.S. degree in electrical engineering in 2017 from Northwestern Polytechnical University, Xi'an, China, and the M.S. degree in electrical engineering in 2020 from Xi'an Jiaotong University, Xi'an, China, where he is currently working toward the Ph.D. degree in electrical engineering.

His current research interests include power electronics, resonant power conversion, and bidirectional dc/dc converters.

Yunqing Pei (Member, IEEE) was born in 1969. He received the B.S. and M.S. degrees in 1991 and 1994, respectively, both in electrical engineering, and the Ph.D. degree in power electronics in 1999, all from Xi'an Jiaotong University, Xi'an, China.

He became a faculty member with Xi'an Jiaotong University, where he is currently a Professor with Xi'an Jiaotong University. From 2006 to 2007, he was a Visiting Scholar with the Center of Power Electronics Systems, Virginia Polytechnic Institute and State University. His research interests include high-power inverters, switch mode power supply, and converters in distributed generation systems.

Laili Wang (Senior Member, IEEE) received the B.S., M.S., and Ph.D. degrees in electrical engineering from the School of Electrical Engineering, Xi'an Jiaotong University, Xi'an, China, in 2004, 2007, and 2011, respectively.

Since 2011, he has been a Postdoctoral Research Fellow with the Department of Electrical Engineering, Queen's University, Kingston, ON, Canada. From 2014 to 2017, he was an Electrical Engineer with Sumida, Kingston, ON, Canada. In 2017, he became a Full Professor with Xi'an Jiaotong University. His research interests include widebandgap power devices, package and integration, high-density power conversion, wireless power transfer, and energy harvesting.

Dr. Wang was a recipient of the Outstanding Youth Award from China Power Supply Society (CPSS), the China Electric Power Excellent Young Technological Talent Award from the Chinese Society of Electrical Engineering, and the Gold Medal Award of Geneva Inventions. He is currently an Associate Editor for IEEE TRANSACTIONS ON POWER ELECTRONICS and IEEE JOURNAL OF EMERGING AND SELECTED TOPICS IN POWER ELECTRONICS. He is the Co-Chair of the System Integration and Application in International Technology Roadmap for Wide Band-Gap Power Semiconductor (ITRW) and the Chair of CPSS and IEEE PELS Joint Chapter in Xi'an, China.

Long Pei (Member, IEEE) was born in Hunan, China, in 1995. He received the B.S. degree in electrical automatization in 2018 from Xi'an Jiaotong University, Xi'an, China, where he is currently working toward the Ph.D. degree in electrical engineering and automation.

His research interests include the design and control of dc/dc resonant power converters and power factor correction ac/dc converters.

Zhixiang Li (Member, IEEE) was born in Shandong, China, in 1996. He received the B.S. degree in electrical engineering in 2019 from Xi'an Jiaotong University, Xi'an, China, where he is currently working toward the Ph.D. degree in electrical engineering.

His research interests include the topology, control, and design of multilevel converters and isolated dc/dc converters, especially the control and design of power electronic transformers, the modular multilevel converter, and the dual-active-bridge converter.

Wei Cao (Member, IEEE) was born in Hebei, China, in 1998. He received the B.S. degree in electrical engineering from Northwestern Polytechnical University, Xi'an, China, in 2020. He is currently working toward the Ph.D. degree in electrical engineering with Xi'an Jiaotong University, Xi'an, China.

His current research interests include high-frequency resonant converters, wide-range dc/dc conversion, and control techniques.